

Cite this: *Chem. Sci.*, 2021, 12, 6772

All publication charges for this article have been paid for by the Royal Society of Chemistry

# Capture of toxic gases in MOFs: SO<sub>2</sub>, H<sub>2</sub>S, NH<sub>3</sub> and NO<sub>x</sub>

Eva Martínez-Ahumada,<sup>a</sup> Mariana L. Díaz-Ramírez,<sup>b</sup> Miriam de J. Velásquez-Hernández,<sup>c</sup> Vojtech Jancik<sup>\*de</sup> and Ilich A. Ibarra<sup>\*a</sup>

MOFs are promising candidates for the capture of toxic gases since their adsorption properties can be tuned as a function of the topology and chemical composition of the pores. Although the main drawback of MOFs is their vulnerability to these highly corrosive gases which can compromise their chemical stability, remarkable examples have demonstrated high chemical stability to SO<sub>2</sub>, H<sub>2</sub>S, NH<sub>3</sub> and NO<sub>x</sub>. Understanding the role of different chemical functionalities, within the pores of MOFs, is the key for accomplishing superior captures of these toxic gases. Thus, the interactions of such functional groups (coordinatively unsaturated metal sites,  $\mu$ -OH groups, defective sites and halogen groups) with these toxic molecules, not only determines the capture properties of MOFs, but also can provide a guideline for the design of new multi-functionalised MOF materials. Thus, this perspective aims to provide valuable information on the significant progress on this environmental-remediation field, which could inspire more investigators to provide more and novel research on such challenging task.

Received 19th March 2021

Accepted 28th April 2021

DOI: 10.1039/d1sc01609a

rsc.li/chemical-science

## 1. Introduction

The accelerated growth of our modern society demands huge amounts of energy. Unwittingly, in order to provide these high energetic levels, an indiscriminate combustion of large volumes of fossil fuels occurs, leading to an incommensurable release of toxic pollutants to the atmosphere. Emissions of anthropogenic air pollutants generate a vast range of health complications (e.g., premature death and morbidity). Additionally, these air pollutants are also responsible for the reduction of the biodiversity, crop damages and acidification of soils and waters.<sup>1</sup> As an example of the adverse impacts to humans, the World Health Organization (WHO) recently announced that air pollution was responsible for the premature mortality of approximately 4.2 million people in 2016 alone.<sup>2</sup> In fact, air pollution is now the single largest environmental health risk worldwide since it is responsible for one in eight premature global deaths.<sup>3</sup> For example, PM<sub>2.5</sub> (fine inhalable particles, with diameters that are

generally 2.5 micrometres and smaller) are responsible for approximately half of the deaths related to air pollution.<sup>4</sup> Thus, PM<sub>2.5</sub> have been classified as the air pollutant with the highest impact in premature mortality,<sup>5</sup> and a reduction of their emissions is crucial. Such reduction can be achieved in two steps: (i) mitigation of primary PM<sub>2.5</sub> emissions and (ii) extenuation of secondary inorganic aerosols (SIA); which are oxidised from precursor emissions such as sulphur dioxide (SO<sub>2</sub>), nitrogen oxides (NO<sub>x</sub>), ammonia (NH<sub>3</sub>) and volatile organic compounds (VOCs).<sup>6</sup> Thus, in order to extenuate these emissions, different actions have been taken, such as the shutdown of some coal-fired power plants and their replacement by thermoelectric power plants, importing electricity from other countries with strict restrictions on the electricity production and the use of more environmentally friendly energy sources.<sup>7</sup> In addition to these actions, the development of efficient technologies for the capture of toxic gases (e.g., NO<sub>x</sub>, SO<sub>2</sub>, NH<sub>3</sub> and H<sub>2</sub>S) from static and mobile sources is necessary, in order to achieve a cleaner environment.<sup>8</sup>

Porous metal-organic frameworks (MOFs) or porous coordination polymers (PCPs) are amongst the most promising candidates for the capture of these toxic gases since their sorption selectivity is directly tuneable as a function of the topology and chemical composition of the pores.<sup>9</sup> Undoubtedly, for NO<sub>x</sub>, SO<sub>2</sub>, NH<sub>3</sub> and H<sub>2</sub>S capture, there is a substantial emphasis on optimising the interactions between MOF materials and these toxic molecules, leading to the discovery of new functional porous materials with enhanced gas adsorption properties.<sup>10</sup> Although MOF materials have shown very promising capabilities for the capture of these toxic gases, their main

<sup>a</sup>Laboratorio de Físicoquímica y Reactividad de Superficies (LaFRS), Instituto de Investigaciones en Materiales, Universidad Nacional Autónoma de México, Circuito Exterior s/n, CU, Del. Coyoacán, 04510, Ciudad de México, Mexico. E-mail: argel@unam.mx; Fax: +52(55) 5622-4595

<sup>b</sup>Department of Chemistry, Mississippi State University, Box 9573, Mississippi 39762, USA

<sup>c</sup>Institute of Physical and Theoretical Chemistry, Graz University of Technology, 8010 Graz, Austria

<sup>d</sup>Universidad Nacional Autónoma de México, Instituto de Química, Ciudad Universitaria, Ciudad de México, Mexico. E-mail: vjancik@unam.mx

<sup>e</sup>Centro Conjunto de Investigación en Química Sustentable UAEM-UNAM, Carr. Toluca-Atlaquilco Km 14.5, Toluca, Estado de México 50200, Mexico

drawback is their vulnerability to these highly corrosive molecules capable of compromising the chemical stability of the MOFs.  $\text{NO}_x$ ,  $\text{SO}_2$ ,  $\text{NH}_3$  and  $\text{H}_2\text{S}$  can disrupt the coordination bonds between the organic ligands (*e.g.*, carboxylate) and the metal centres, occasioning the breakdown of the MOF structure. Therefore, chemical stability of the MOFs is a fundamental requirement for the capture of these toxic gases. The present contribution aims to provide a useful reference in the field of capturing toxic gases in MOFs, emphasising on their chemical stability and the role of the functional groups to enhance such captures. We hope to encourage more research groups to explore the exciting frontiers of science in environmental-remediation applications for MOFs.

## 2. Sulphur dioxide

The anthropogenic release of  $\text{SO}_2$  into the atmosphere is mainly due to the combustion of fossil fuels (*e.g.*, electric power generation). One of the first environmental problems related to  $\text{SO}_2$  was observed during the last century in the acidic deposition.<sup>11</sup> To avoid this, since 1990 many European countries have considerably reduced their  $\text{SO}_2$  emissions.<sup>12</sup> Nevertheless, the rapid industrialisation of some developing countries has caused a constant presence of  $\text{SO}_2$  in the atmosphere,<sup>13</sup> risking the health of millions of people (*vide supra*).

$\text{SO}_2$  is a colourless, non-flammable and corrosive gas with high solubility ( $120 \text{ g l}^{-1}$ ) in water. Among the technologies for  $\text{SO}_2$  capture, wet and dry flue-gas desulfurization (FGD) processes are commonly used,<sup>14</sup> where the cost and recyclability depend on the used technology. Among them, alkaline solutions, activated carbons, zeolites and silica have typically showed low  $\text{SO}_2$  adsorption capacities, accompanied by the corrosion of pipelines and high energy regeneration overheads.<sup>15</sup> Thus, the design of new materials is extremely necessary in order to meet all the challenges that the capture of  $\text{SO}_2$  signifies. MOF materials are an exciting alternative for the capture of  $\text{SO}_2$  as they have demonstrated promising results for the  $\text{SO}_2$  capture assignment, mainly due to their specific chemical functionality and pore dimensions.<sup>16</sup> The following section focuses on the highlights of remarkable MOF materials stable towards  $\text{SO}_2$ , with the emphasis not only on their capture performance, but also on showing the role of different chemical functionalities which are the key for the  $\text{SO}_2$  capture.

### 2.1 MOFs for $\text{SO}_2$ capture

The chemical nature of the  $\text{SO}_2$  molecule and its main binding modes: oxygen, an electron-rich atom that can act as a Lewis base; and sulphur that can be a Lewis acid site, have been exploited to improve its adsorption on the porous surface of the MOFs. Due to the specific functionalisation of these MOFs, interesting  $\text{SO}_2$  capture results have been achieved. Such functionalisation can be classified in four main categories: (i) coordinatively unsaturated metal sites (open metal sites), (ii)  $\mu\text{-OH}$  groups, (iii) defective sites and (iv) halogen functionalisation.

**(i) Coordinatively unsaturated metal sites.** Although some research has proven the capture of  $\text{SO}_2$  by different MOFs, the majority of these examples have shown to be chemically unstable upon  $\text{SO}_2$  exposure.<sup>17</sup> For example, MOF-177 (an open  $\text{Zn}^{2+}$  sites system reported by Janiak and co-workers<sup>18</sup>) holds the  $\text{SO}_2$  capture record ( $25.7 \text{ mmol g}^{-1}$  at 298 K and 1 bar) but suffers a partial structural degradation, after the exposure to  $\text{SO}_2$ , as demonstrated by PXRD and a significant BET surface area reduction.<sup>18</sup> Conversely, MFM-170 an open  $\text{Cu}^{2+}$  sites MOF;  $[\text{Cu}_2(\text{L})]$  ( $\text{H}_4\text{L} = 4',4'''$ -(pyridine-3,5-diyl)bis([1,1'-biphenyl]-3,5-dicarboxylic acid)), not only demonstrated to be highly stable to  $\text{SO}_2$  ( $17.5 \text{ mmol g}^{-1}$  at 298 K and 1 bar), but also to humid  $\text{SO}_2$ .<sup>19</sup> Yang and Schröder elegantly demonstrated the reversible coordination of  $\text{SO}_2$  to open  $\text{Cu}^{2+}$  sites in MFM-170 by *in situ* synchrotron single-crystal X-ray diffraction, *in situ* FTIR spectroscopy and *in situ* inelastic neutron scattering (INS).<sup>19</sup> In brief, all of this comprehensive experimental evidence corroborated that the  $\text{Cu}^{2+}$  site is the thermodynamically strongest  $\text{SO}_2$  binding site (see Fig. 1), but is sufficiently weak to be almost entirely desorbed upon reducing the pressure. The material can also be fully regenerated by heating to 400 K without any loss of crystallinity even after completing fifty  $\text{SO}_2$  adsorption-desorption cycles at 298 K.<sup>19</sup>

Our group reported a partially fluorinated version of MIL-101(Cr) named MIL-101(Cr)-4F(1%).<sup>20</sup> The particularity of MIL-101(Cr)-4F(1%) is the different chemical character of the  $\text{Cr}^{3+}$  metal centres, in comparison to MIL-101(Cr). The incorporation of fluorine in MIL-101(Cr) promoted a higher acidity of some of the  $\text{Cr}^{3+}$  metal centres (open metal sites), due to the capability of fluorine to attract electrons.<sup>20</sup> Such difference afforded a total



Fig. 1  $\text{SO}_2$  positions within MFM-170 pores obtained from *in situ* single-crystal X-ray diffraction. Purple  $\text{SO}_2$  molecule is located at the thermodynamically strongest binding site. Cu, cyan; C, black; O, red; N, blue. Reprinted (adapted) with permission from ref. 19. Copyright (2019) Springer Nature.



SO<sub>2</sub> capture of 18.4 mmol g<sup>-1</sup> at 298 K and up to 1 bar, chemical stability towards dry and humid SO<sub>2</sub> and an exceptional cycling performance with facile regeneration.<sup>20</sup>

This uptake represents the highest SO<sub>2</sub> capture for a structurally stable MOF material. In addition, *in situ* DRIFT spectroscopy upon the adsorption of CO demonstrated the efficient packing of SO<sub>2</sub> molecules within MIL-101(Cr)-4F(1%). Thus, the SO<sub>2</sub> uptake mechanism takes place in three stages: (i) adsorption at acid (Lewis) Cr<sup>3+</sup> sites with a relatively high heat of adsorption for SO<sub>2</sub>; (ii) adsorption at both acid (Lewis and Brønsted) sites of MIL-101(Cr)-4F(1%) and (iii) adsorption within the cavities of this MOF material. Up to this point, we have presented three examples (MOF-177, MFM-170 and MIL-101(Cr)-4F(1%)) of MOF materials with coordinatively unsaturated metal sites that demonstrated the highest SO<sub>2</sub> captures for any MOF. One material (MOF-177) demonstrated poor structural stability towards SO<sub>2</sub> versus the high structural stability of MFM-170 and MIL-101(Cr)-4F(1%) in the presence of SO<sub>2</sub> and humid SO<sub>2</sub>. Unwittingly, the fundamental question arises: why is MOF-177 unstable while MFM-170 and MIL-101(Cr)-4F(1%) are stable to SO<sub>2</sub>? In order to answer this question, their comparison is presented in Table 1, allowing to propose a stability hypothesis for these materials.

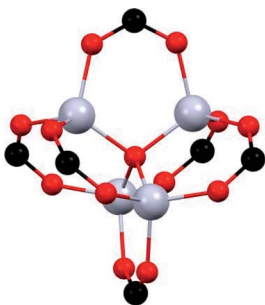
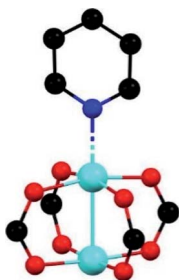
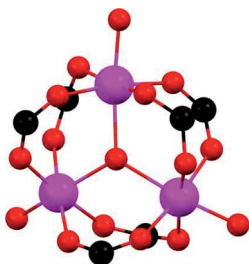
The design of stable frameworks for capture, confinement and release of corrosive gases uses tools centred in the robustness of the metal-linker bond, the use of inert or higher-valent metals and, the use of poly-nuclear secondary building units (SBUs).<sup>21</sup> In the case of MOF-177, MFM-170 and MIL-101(Cr)-4F(1%), these exhibit at least one of such design tools. These three MOFs are composed of carboxylate ligands and robust SBUs, this multinuclearity gives, in theory, a better thermal and chemical stability. Nonetheless, in the case of MOF-177,<sup>18</sup> that possess the highest BET surface area, pore volume and the

record of SO<sub>2</sub> capture, the use of robust polynuclear cluster [Zn<sub>4</sub>(μ<sub>4</sub>-O)(O<sub>2</sub>CR)<sub>6</sub>] (see comparative Table 1), is not enough to achieve a reversible SO<sub>2</sub> adsorption and the framework suffers a partial decomposition.

This result is most likely due to the propensity of the Zn–O bond to bind SO<sub>2</sub> and form SO<sub>3</sub><sup>2-</sup>. Similar behaviour was observed on a ZnO surface exposed to SO<sub>2</sub> gas, that reacts with the oxygen atoms from the Zn–O bonds forming the SO<sub>3</sub><sup>2-</sup> and SO<sub>4</sub><sup>2-</sup> species.<sup>22,23</sup> In fact, other Zn-based MOFs that have been studied for SO<sub>2</sub> adsorption have shown similar stability problems. This is also the case of Zn-MOF-74 (ref. 24) with a rod-like SBU and coordinatively unsaturated zinc sites, where a Zn⋯O=S=O interaction leads to a chemisorption. Additionally, materials with paddlewheel SBUs, such as Zn<sup>2+</sup>-BDC (MOF-2) where the catalytic oxidation of SO<sub>2</sub> under humid conditions was confirmed by the presence of sulphate species.<sup>25</sup> Conversely, when the coordinatively unsaturated zinc site is blocked (*i.e.*, pillared MOFs), direct interaction of adsorbate with the metal centre is not observed, as for example in Zn(bdc)(ted)<sub>0.5</sub> (ref. 26) and Zn-DMOF.<sup>27</sup> These comparative results suggest that in the case of Zn-based materials, the robustness of the SBU plays a secondary role in chemical stability against SO<sub>2</sub>, and the fact that they are constructed from a divalent metal that forms labile bonds,<sup>28</sup> makes them more susceptible to collapse.

Although MFM-170 contains the Cu<sup>2+</sup> paddlewheel SBU, a cluster frequently instable under harsh conditions such as corrosive or acidic gases,<sup>29,30</sup> it is stable even after 50 adsorption–desorption cycles of SO<sub>2</sub>.<sup>19</sup> This extraordinary chemical stability is mainly due to two important factors: (i) the unusual paddlewheel SBU formed in the framework and (ii) additional intermolecular interactions formed between SO<sub>2</sub> and the pore-walls of the framework. The di-cooper paddlewheel SBU shows the particularity of only one of the Cu<sup>2+</sup> centres axially

Table 1 Comparison of structural characteristics in metal–organic frameworks with the highest SO<sub>2</sub> capture

Material	MOF-177	MFM-170	MIL-101(Cr)-4F(1%)
Ligand	H <sub>3</sub> BTB	H <sub>4</sub> L = 4',4'''-(pyridine-3,5-diyl)bis([1,1'-biphenyl]-3,5-dicarboxylic acid)	H <sub>2</sub> BDC/H <sub>2</sub> BDC-4F
SBU	[Zn <sub>4</sub> (μ <sub>4</sub> -O)(O <sub>2</sub> CR) <sub>6</sub> ]	[Cu <sub>2</sub> (O <sub>2</sub> CR) <sub>4</sub> ]	[Cr <sub>3</sub> (μ <sub>3</sub> -O)(O <sub>2</sub> CR) <sub>6</sub> ]
			
BET surface area [m <sup>2</sup> g <sup>-1</sup> ]	4100	2408	2176
Pore volume [cm <sup>3</sup> g <sup>-1</sup> ]	1.51	0.88	1.19
SO <sub>2</sub> adsorption [mmol g <sup>-1</sup> ]	25.7	17.5	18.4
Packing density [cm <sup>3</sup> g <sup>-1</sup> ]	1.09	1.27	1.00
Stability under SO <sub>2</sub>	Partial destruction after SO <sub>2</sub> exposure	Stable after 50 cycles	Stable after 50 cycles



coordinated to a nitrogen atom from the pyridyl-based ligand, leaving the other  $\text{Cu}^{2+}$  metal centre coordinatively unsaturated and pointing toward the centre of the pore (Table 1). The effect of this structural arrangement is evident on the high  $\text{SO}_2$  uptake, where the  $\text{Cu}^{2+}$  sites are able to fix  $\text{SO}_2$  by forming a strong Cu–O bond without ligand displacement. Such behaviour was previously observed in a  $\text{Cu}^{2+}$ -BDC MOF material.<sup>25</sup> It is significant that this interaction does not represent the main  $\text{SO}_2$  binding site due to the steric hindrance generated by a neighbouring  $\text{SO}_2$  molecule. This latter molecule has several interactions: (i) with the C–H portion of the ligand, (ii) with the oxygen atoms in the paddlewheel SBU, and (iii) with other  $\text{SO}_2$  molecules. All these interactions promote an efficient packing within the pore surface, maximising the adsorbate–adsorbent bonds and presumably avoids the frame destruction. Both materials reviewed above, MOF-170 and MFM-177, are formed by first-row transition metals  $\text{Zn}^{2+}$  and  $\text{Cu}^{2+}$ , respectively, and follow the stability order of the Irving–Williams series for divalent metals:  $\text{Mn} < \text{Fe} < \text{Co} < \text{Ni} < \text{Cu} > \text{Zn}$ .<sup>31</sup> Thus, the high  $\text{SO}_2$  capture can be attributed to the large BET surface area and pore size rather than to the local pore environment, while structural stability is associated with the type of metal, and the interactions adsorbate–adsorbent.

Additionally, the use of higher-valent metal ions such as  $\text{Al}^{3+}$ ,  $\text{Sc}^{3+}$ ,  $\text{Cr}^{3+}$  or  $\text{Zr}^{4+}$  allows the formation of stronger M–O bonds with carboxylate ligands compared to divalent ions.<sup>21</sup> Thus, the lability of metal–ligand bonding is higher in  $\text{Cu}^{2+}$  or  $\text{Zn}^{2+}$ -based MOFs than  $\text{Cr}^{3+}$  MOFs. As a consequence, MOFs constructed from divalent metals such  $\text{Cu}^{2+}$  and  $\text{Zn}^{2+}$ , typically show partial or total degradation under harsh conditions.<sup>32</sup> Due to the inertness of the Cr–O bond,  $\text{Cr}^{3+}$ -based MOFs highly resistant to the attack of acid and base guests were reported.<sup>33,34</sup> As described above, the third material, MIL-101(Cr)-4F(1%), has the highest  $\text{SO}_2$  adsorption among  $\text{SO}_2$ -stable MOFs.<sup>20</sup> This framework poses a robust trinuclear metal cluster with coordinatively unsaturated chromium sites after the activation process (Table 1). When comparing MIL-101(Cr)-4F(1%) to MFM-170, both materials stable towards  $\text{SO}_2$ , we can observe that the  $\text{Cr}^{3+}$  is harder than  $\text{Cu}^{2+}$  ions according to the Pearson acid–base concept<sup>35</sup> and therefore the coordinated bond with carboxylic ligands is stronger for the trivalent cation than for the divalent cation. However, the  $\text{Cu}^{2+}$  paddlewheel increases its stability when the N-containing ligand coordinates to one of the  $\text{Cu}^{2+}$  ions.<sup>36</sup>

**(ii)  $\mu$ -OH groups.** This particular hydroxo-functionalisation in MOF materials is well exemplified by the MFM-300(M) (MFM = Manchester Framework Material, M =  $\text{Al}^{3+}$ ,  $\text{In}^{3+}$ ,  $\text{Ga}^{3+}$  and  $\text{Sc}^{3+}$ ) family. These outstanding MOF materials are chemically stable towards  $\text{SO}_2$  and have been reported by Schröder and Yang.<sup>37</sup> The general chemical formula of this group of MOFs is  $[\text{M}_2(\text{OH})_2(\text{L})]$  ( $\text{H}_4\text{L}$  = biphenyl-3,3',5,5'-tetracarboxylic acid =  $\text{C}_{16}\text{O}_8\text{H}_6$ ). MFM-300(M) shows a 3D open framework which contains  $[\text{MO}_4(\text{OH})_2]$  octahedra connected *via* the *cis*- $\mu$ -OH groups into infinite chains, and further coordinated by the tetradentate ligand ( $\text{L}^{4-}$ ). This particular organisation produces highly porous materials (see Table 2), well defined by one-dimensional pore channels organized in a “wine rack” display.

The first MFM-300 material investigated for the capture of  $\text{SO}_2$  was MFM-300(Al).<sup>37a</sup> Although the  $\text{SO}_2$  capture was not remarkably high (see Table 2), the identification of the preferential  $\text{SO}_2$  adsorption sites was achieved by sophisticated *in situ* INS and PXRD experiments, revealing that the  $\mu$ -OH groups bind  $\text{SO}_2$  molecules through the formation of  $\text{O}=\text{S}=\text{O}(\delta^-)\cdots\text{H}(\delta^+)-\text{O}$  hydrogen bonds, reinforced by weak supramolecular interactions with C–H atoms from the aromatic rings of the framework (Fig. 2).<sup>37a</sup> In the case of MFM-300(In) (also known as InOF-1 (ref. 38)) the  $\text{SO}_2$  uptake was slightly higher than for MFM-300(Al) (see Table 2), and *in situ* INS and PXRD experiments corroborated the same preferential adsorption site for  $\text{SO}_2$  (see Fig. 3) with exceptional chemical stability for  $\text{SO}_2$  capture under both dry and humid conditions.<sup>37b</sup> In fact, Eddaoudi and Salama fabricated an advanced chemical capacitive sensor, using MFM-300(In), for the detection of very low concentrations of  $\text{SO}_2$  ( $\approx 5$  ppb) at room temperature.<sup>39</sup>

MFM-300(Sc) showed the highest  $\text{SO}_2$  uptake of the MFM-300(M) materials (see Table 2), Grand Canonical Monte Carlo (GCMC) simulations demonstrated the same preferential adsorption sites ( $\mu$ -OH) and by confining small amounts of EtOH (2.6 wt%) the  $\text{SO}_2$  capture increased by 40% (see Fig. 4).<sup>37c</sup> The only MFM-300 remaining to be investigated in the capture of  $\text{SO}_2$  is MFM-300(Ga),<sup>37d</sup> where we anticipate, based on the pore volume, performance similar to MFM-300(Sc).

Thus, the MFM-300(M) MOF materials have shown the relevance of the hydroxo-functionalisation to the capture and detection of  $\text{SO}_2$  with high chemical stability and excellent cyclability involving a remarkably facile regeneration. The key for all of such outstanding properties is the strength of the coordination bonds between the oxygen atoms form the

Table 2 Comparison of MFM-300(M) family

Metal center (M)	BET Surface area [ $\text{m}^2 \text{g}^{-1}$ ]	Pore volume [ $\text{cm}^3 \text{g}^{-1}$ ]	$\text{SO}_2$ adsorption [ $\text{mmol g}^{-1}$ ]	Packing density [ $\text{g cm}^{-3}$ ]	$Q_{\text{st}}$ [ $\text{kJ mol}^{-1}$ ]	Stability
Al	1370	0.375	7.1	1.213	31.25 <sup>a, 37e</sup>	Stable over 4 years of exposure
In	1071	0.419	8.28	1.266	34.5	Stable in dry and humid conditions
Ga	1045	0.62	—	—	—	—
Sc	1360	0.56	9.4	1.075	36.2	Stable in dry and humid conditions/over 10 cycles

<sup>a</sup> Adsorption near the zero-coverage calculated by GCMC.







Fig. 2 Preferred binding sites for  $\text{SO}_2$  molecules inside MFM-300(Al) determined by *in situ* PXRD. (I) Moderated hydrogen bond. (II) Weak hydrogen bond. Reprinted (adapted) with permission from ref. 37a. Copyright (2012) Springer Nature.



Fig. 3 Binding sites for  $\text{SO}_2$  molecules within MFM-300(In) determined by single-crystal X-ray diffraction (a), and DFT calculations (b). Reprinted (adapted) with permission from ref. 37b. Copyright (2016) John Wiley & Sons.

carboxylic ligand (biphenyl-3,3',5,5'-tetracarboxylic acid) and the  $\text{M}^{3+}$  metal centres. The ionic radii of  $\text{Al}^{3+}$ ,  $\text{In}^{3+}$  and  $\text{Sc}^{3+}$  cations, in octahedral coordination, are 0.675, 0.940 and 0.885 Å, respectively.<sup>40a</sup>

This leads to a higher surface charge density for the  $\text{Al}^{3+}$  metal centre and, therefore, the M–O bond strength decreases



Fig. 4  $\text{SO}_2$  adsorption isotherm of scandium-based MFM-300 (blue isotherm) and after confinement of 2.8% EtOH (red isotherm). Reprinted with permission from ref. 37c. Published (2019) by The Royal Society of Chemistry.

in this order:  $\text{Al}^{3+} > \text{Sc}^{3+} > \text{In}^{3+}$ . Thus, a higher ligand exchange can occur in the In-based complex.<sup>40b</sup> However, MFM-300(In) does not suffer apparent displacement of carboxylate ligands after  $\text{SO}_2$  exposure. In the MFM-300(M) family all the metal cations are nonmagnetic because of all paired electrons,<sup>41</sup> and the comparison between octahedral complexes formed by trivalent cations of group 13 such as  $\text{Al}^{3+}$ ,  $\text{Ga}^{3+}$  and  $\text{In}^{3+}$ , with the transition-metal analogue  $\text{Sc}^{3+}$ , has shown that in the group 13 metal complexes the d orbitals are not involved in the metal-linker bonding due to their high energy ( $3d^{10}$  and  $4d^{10}$  configuration). In the case of  $\text{Sc}^{3+}$ , a complex with  $12e^-$ , d orbitals form part of the M–O bonds (Fig. 5a). On the other hand, these types of complexes are considered as electron-rich hypervalent species with 7-center-12-electron bonding pattern (Fig. 5b).<sup>40c</sup> This type of binding confers to the group 13 complexes thermal stability and in this particular case, the kinetic stability is comparable to that of the transition metal analogues. At this point, we can corroborate that frameworks constructed with trivalent cations are more stable than MOFs based on divalent cations (considering the stability of Irving–Williams series discussed above), as well that carboxylate ligands form with  $\text{M}^{3+}$  cations stronger bonds than divalent cations with N-based ligands.<sup>32</sup>

**(iii) Defective sites.** Crystal irregularities (composition inhomogeneities or defects) are fundamental characteristics of some solid-state materials and provide very particular physical and chemical properties.<sup>42</sup> Such defects do not necessarily mean adverse effects. Due to their extraordinary modularity and tunability, MOFs allow the introduction of different kinds of defects while maintaining the overall structure integrity. Typically, “defective MOFs” have showed extraordinary superior catalysis performances,<sup>43</sup> while Navarro and co-workers have taken a step forward and elegantly demonstrated the self-detoxification of defective UiO-66 examples to filter chemical-



Fig. 5 Schematic MO diagrams for an  $O_h$ -symmetric  $12e^-$  complex with d orbitals (a, red) and the MO diagram without d orbitals in 7c- $12e^-$  pattern of MO (b, blue). Reprinted (adapted) with permission from ref. 40c. Copyright (2015) John Wiley & Sons.

warfare agents.<sup>44</sup> In the case of SO<sub>2</sub>, the same research group reported on the increase of the SO<sub>2</sub> adsorption capacities, energies and SO<sub>2</sub>/CO<sub>2</sub> selectivity for defective nickel pyrazolate MOF materials, prepared by introducing extra-framework Ba<sup>2+</sup> ions into the porous structure and ligand functionalisation.<sup>45</sup>

Thus, the post-synthetic treatment of the [Ni<sub>8</sub>(OH)<sub>4</sub>(H<sub>2</sub>O)<sub>2</sub>(BDP\_X)<sub>6</sub>] (H<sub>2</sub>BDP\_X = 1,4-bis(pyrazol-4-yl) benzene-4-X with X = H (1), OH (2), NH<sub>2</sub> (3)) systems with ethanolic solutions of potassium hydroxide leads to the formation of defective K [Ni<sub>8</sub>(OH)<sub>3</sub>(EtO)<sub>3</sub>(BDP\_X)<sub>5.5</sub>] (1@KOH, 3@KOH) and K<sub>3</sub>[Ni<sub>8</sub>(OH)<sub>3</sub>(EtO)(BDP\_O)<sub>5</sub>] (2@KOH).<sup>46</sup> Exposing the 1@KOH–3@KOH materials to aqueous Ba(NO<sub>3</sub>)<sub>2</sub> solutions incorporates barium cations into the solution, yielding the defective ion exchanged Ba<sub>0.5</sub>[Ni<sub>8</sub>(OH)<sub>3</sub>(EtO)<sub>3</sub>(BDP\_X)<sub>5.5</sub>] (1@Ba(OH)<sub>2</sub>, X = H; 3@Ba(OH)<sub>2</sub>, X = NH<sub>2</sub>), and Ba<sub>1.5</sub>[Ni<sub>8</sub>(OH)<sub>3</sub>(EtO)(BDP\_O)<sub>5</sub>] (2@Ba(OH)<sub>2</sub>) systems.<sup>45</sup> Interestingly, density functional theory (DFT) calculations located the extra-framework cations close to the crystal defect sites (Fig. 6a). In addition, DFT results demonstrated that the average 3D structure of the MOF framework is preserved.<sup>45</sup> SO<sub>2</sub> dynamic adsorption experiments confirmed the beneficial influence of the deliberate introduction of defects by a subsequent K<sup>+</sup> to Ba<sup>2+</sup> ion exchange process on the SO<sub>2</sub> capture.<sup>45</sup> The authors demonstrated that the pre-synthetic introduction of amino and hydroxyl functional groups on the organic linkers and the post-synthetic modifications, synergistically increase the SO<sub>2</sub> capture capacity of these materials. In addition, chemisorption of SO<sub>2</sub> was observed in all the systems: after all available sites for SO<sub>2</sub> chemisorption were occupied, during the first exposure, reversible adsorption takes place in a steady way

evidencing the stability of the materials upon continuous SO<sub>2</sub> exposure. This high affinity of these MOF materials for SO<sub>2</sub> was attributed to the increased basicity of the nickel hydroxide clusters after the introduction of defects. Lewis acid–base interactions with SO<sub>2</sub> molecules can afford the formation of HSO<sub>3</sub><sup>−</sup> and SO<sub>3</sub><sup>2−</sup> species according to eqn (1):



Furthermore, the existence of extra-framework cations located close to defects sites promotes the formation of more stable MSO<sub>3</sub> (M = Ba, 2 K) sulphite species according to eqn (2):



These chemisorption mechanisms were supported by the DFT simulations (Fig. 6), showing that 1@Ba(OH)<sub>2</sub> establishes stronger interactions with SO<sub>2</sub> molecules than 1@KOH due to the specific interactions with extra-framework barium cations.

Thus, this sophisticated and comprehensive study, by Navarro *et al.*,<sup>45</sup> carefully incorporated essential variables to improve the SO<sub>2</sub> capture performance of these MOF materials. Such variables play together to increase the interaction with SO<sub>2</sub> and can be summarised as (i) enhanced basicity of metal hydroxide clusters as a result of additional hydroxide anions replacing the missing linkers defects; (ii) affinity of extra-framework Ba<sup>2+</sup> ions for SO<sub>2</sub> sequestration; (iii) higher pore accessibility of the 3-D structure due to missing linker defects and (iv) the fine-tuning of the pore surface polarity by the benzene functional groups.

The post-synthetic inclusion of Ba<sup>2+</sup> cations to improve the SO<sub>2</sub> adsorption was later validated by Navarro and co-workers<sup>47</sup> in the Ni-based MOF material Ni<sub>2</sub><sup>2+</sup>{Ni<sub>4</sub><sup>2+</sup>[Cu<sub>4</sub><sup>2+</sup>–(Me<sub>3</sub>mpba)<sub>2</sub>]<sub>3</sub>}·54H<sub>2</sub>O (1). In this case, the exchange of the Ni<sup>2+</sup> cations for Ba<sup>2+</sup> was accomplished by soaking 1 in an aqueous solution of Ba(NO<sub>3</sub>)<sub>2</sub> for two days to finally obtain a novel crystalline phase of heterotrimetallic oxamato-based MOF with the formula [Ba<sup>2+</sup>(H<sub>2</sub>O)<sub>4</sub>]<sub>1.5</sub>[Ba<sup>2+</sup>(H<sub>2</sub>O)<sub>5</sub>]<sub>0.5</sub>{Ni<sub>4</sub><sup>2+</sup>[Cu<sub>2</sub><sup>2+</sup>–(Me<sub>3</sub>mpba)<sub>2</sub>]<sub>3</sub>}·57.5H<sub>2</sub>O (2). On this occasion, the presence of the hydrated Ba<sup>2+</sup> counterions within the MOF's pores allowed the SO<sub>2</sub> molecules to interact with the network reversibly *via* Cu<sup>2+</sup>⋯O<sub>SO2</sub> and O<sub>H2O</sub>⋯O<sub>SO2</sub> interactions. The amount of SO<sub>2</sub> adsorbed in 2 increased from 2.0 to 2.5 mmol g<sup>−1</sup> in comparison to 1, respectively. This reversibility was conserved over 10 adsorption–desorption cycles. Theoretical calculations demonstrated that the principal binding site of SO<sub>2</sub> molecules is with coordinated water molecules, and it showed moderate adsorption energy of −65.5 kJ mol<sup>−1</sup>, otherwise, the direct interaction of SO<sub>2</sub> with Ba<sup>2+</sup> cations would induce a higher adsorption energy (>100 kJ mol<sup>−1</sup>) due to the formation of an irreversible bond. Thus, this research group has elegantly proved that the formation of defective sites and the incorporation of large cations such as Ba<sup>2+</sup> is a good and feasible post-synthetic method for modulating the adsorptive capacities of MOF materials.



Fig. 6 DFT structure minimization of molecular configuration of one (a and b) and two (c and d) adsorbed SO<sub>2</sub> molecules on 1@KOH (left) and 1@Ba(OH)<sub>2</sub> (right) materials. For sake of clarity, only the region around the metal cluster is shown. Ni (cyan); K (purple); Ba (wine); C (grey); N (blue); O (magenta); H (white); S (yellow). Reprinted (adapted) with permission from ref. 45. Copyright (2017) Springer Nature.



**(iv) Halogen functionalisation.** Halogen functionalised materials are developing as promising technological platforms for innovative applications in different research fields such as catalysis, environmental remediation, sensing, and energy transformation.<sup>48</sup> On the other hand, cationic or anionic frameworks have shown potential applications in the capture of gases as the ions present inside the pores of the MOFs can be a benefit for the interaction with guest molecules.<sup>49</sup> The presence of halogen counterions in porous materials has demonstrated an enhancement of the SO<sub>2</sub> capture performance due to the involvement of ionic bonding.<sup>50</sup> The following section is devoted to MOFs with halogen ions in their structure that participate in the adsorption of gaseous SO<sub>2</sub>.

Yang and Xing incorporated inorganic hexafluorosilicate (SiF<sub>6</sub><sup>2−</sup>, SIFSIX) anions (as pillars) into a series of MOF materials (SIFSIX-1-Cu, SIFSIX-2-Cu (2 = 4,4′-dipyridylacetylene), SIFSIX-2-Cu-i, SIFSIX-3-Zn (3 = pyrazine), and SIFSIX-3-Ni) and investigated the SO<sub>2</sub> adsorption properties of these materials.<sup>51</sup> The remarkable highly efficient removal of SO<sub>2</sub> from other gases, particularly at a very low SO<sub>2</sub> concentrations, and excellent SO<sub>2</sub>/CO<sub>2</sub> and SO<sub>2</sub>/N<sub>2</sub> selectivities were attributed to the strong electrostatic interactions between the SO<sub>2</sub> molecules and the SiF<sub>6</sub><sup>2−</sup> anions (S<sup>δ+</sup>...F<sup>δ−</sup>), assisted by dipole–dipole interactions with the ligand (O<sup>δ−</sup>...H<sup>δ+</sup>).<sup>51</sup> The authors identified the interactions between the SO<sub>2</sub> molecule and SIFSIX materials by modelling studies using first-principles DFT-D (dispersion-corrected density functional theory) calculations (see Fig. 7).<sup>51</sup> These computational calculations were experimentally corroborated by Rietveld refinement of the powder X-ray diffraction patterns of SO<sub>2</sub>-loaded samples to locate the adsorbed positions of the SO<sub>2</sub> molecules in the crystal structure of SIFSIX materials.<sup>51</sup> Thus, this strategy highlighted the relevance on creating the multiple binding sites (anionic and aromatic linkers) which can originate the specific recognition of SO<sub>2</sub> to optimise its capture.

Similarly, Salama and Eddaoudi demonstrated how fluorinated MOFs (KAUST-7 and KAUST-8) can be formidable candidates for sensing SO<sub>2</sub> from flue gas and air (250 ppm to 7% of SO<sub>2</sub>).<sup>52</sup> SCXRD data collected on the SO<sub>2</sub>-loaded KAUST-7 and KAUST-8 identified the preferential adsorption sites for SO<sub>2</sub>

revealing, comparable to SIFSIX materials, strong electrostatic interactions between the SO<sub>2</sub> molecules and the fluorinated pillars (S<sup>δ+</sup>...F<sup>δ−</sup>), supported by dipole–dipole interactions with the pyrazine ligand (O<sup>δ−</sup>...H<sup>δ+</sup>), see Fig. 8.<sup>52</sup> These interactions were also corroborated by DFT calculations.

Another remarkable halogen functionalisation was presented by Janiak and co-workers,<sup>53</sup> where MOF-801 was modified by reacting zirconium halides (ZrX<sub>4</sub>; X = Cl, Br, I) in water with acetylenedicarboxylic acid. The HX addition and material construction occurred in a one-pot reaction yielding three microporous HHU-2-X MOFs (X = Cl, Br, I). The material HHU-2-Cl showed an increased SO<sub>2</sub> uptake (by 21%) in comparison to the nonhalogenated MOF-801.<sup>53</sup> Therefore, as previously demonstrated by the SIFSIX materials, KAUST-7, and KAUST-8, the electrostatic interactions between the SO<sub>2</sub> molecules and the Cl (S<sup>δ+</sup>...Cl<sup>δ−</sup>), might be responsible for such SO<sub>2</sub> capture enhancement.

### 3. Hydrogen sulphide

H<sub>2</sub>S is released to the environment *via* natural events such as volcanic eruptions, gas streams, hot springs, decomposition of organic matter and bacterial reduction.<sup>54</sup> Additionally, H<sub>2</sub>S is emitted by some chemical industries, *e.g.*, oil desulphurisation processes at oil refineries, burning fossil fuels and mass transportation.<sup>55</sup> H<sub>2</sub>S is a main air pollutant which negative impacts the environment as it is one of the main sources of acid rain,<sup>55</sup> and it is highly toxic to humans (concentrations above 700 ppm in the air can cause death).<sup>56</sup>



Fig. 7 Binding sites for SO<sub>2</sub> molecules adsorbed within SIFSIX-1-Cu determined by DFT-D calculations. Interaction S<sup>δ+</sup>...F<sup>δ−</sup> (a), and dipole–dipole interactions with the ligand O<sup>δ−</sup>...H<sup>δ+</sup> (b). Cu (dark teal); F (red); Si (light blue); C (grey); H (light grey); N (sky blue); O (orange); S (sea green). Reprinted (adapted) with permission from ref. 51. Copyright (2017) John Wiley & Sons.

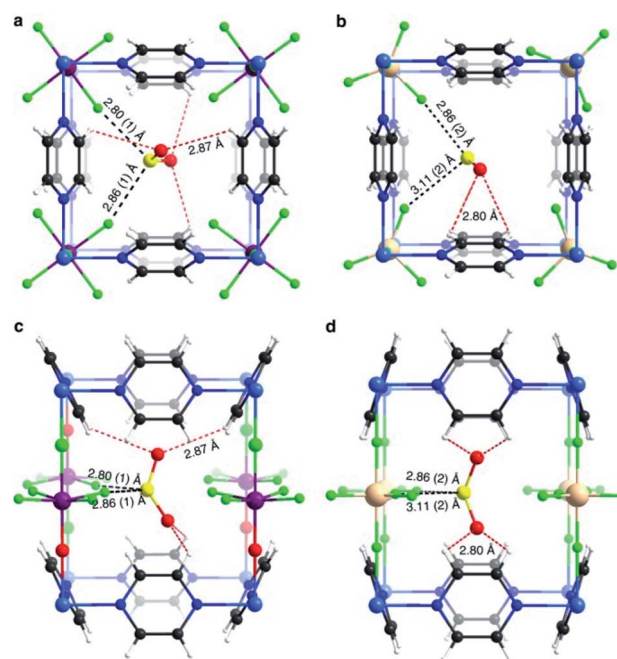


Fig. 8 SO<sub>2</sub> interactions within KAUST-7 (a and c), and KAUST-8 (b and d). Ni (blue light); Nb (purple); Al (beige); F (green); C (black); N (blue); O (red); H (white); S (yellow). Reprinted (adapted) with permission from ref. 52. Copyright (2019) Springer Nature.





H<sub>2</sub>S is a colourless, flammable gas with a characteristic rotten egg odour. Typical strategies to capture H<sub>2</sub>S comprise alkanolamines and ionic liquids, adsorption in solid materials (*i.e.*, zeolites, activated carbons and metal oxides), membrane separation and cryogenic distillation.<sup>57</sup> However, these techniques have major drawbacks, such as low H<sub>2</sub>S capture, corrosion of pipelines and large cost of expenditure and recovery.<sup>58</sup> Thus, the development of new technologies for a dry adsorption process (avoiding solvents/water consumption is essential to reduce waste generation), for removal and capture of H<sub>2</sub>S signifies a technological challenge which could allow not only the capture of H<sub>2</sub>S from the main source, but also its use as feedstock, similarly to the CO<sub>2</sub> technologies (CCS).<sup>59</sup> MOFs have been visualised for the capture of H<sub>2</sub>S; however, most of them have shown poor chemical stability in its presence.<sup>60</sup> Nonetheless, chemically stable MOF materials have demonstrated promising results in the reversible capture of H<sub>2</sub>S.<sup>61</sup> This section highlights outstanding MOF materials that have shown high H<sub>2</sub>S capture performances and *in situ* H<sub>2</sub>S transformations, as well as biomedical applications.

### 3.1 MOFs for H<sub>2</sub>S capture

Distinctive investigations reported by De Weireld,<sup>62</sup> Zou<sup>63</sup> and Eddaoudi<sup>64</sup> reveal that the majority of MOF materials experience structural decomposition upon adsorption of H<sub>2</sub>S or the desorption of it resulted complicated, due to relatively strong host–guest binding in the pores (strong physisorption or chemisorption). In such cases, the reactivation of the materials involves a large energy penalty or is not feasible. Thus, the identification of new MOFs capable of capturing H<sub>2</sub>S under industrially practical pressure-swing desorption conditions,<sup>65</sup> represents a very important challenge to solve. This perspective focused on (i) high and reversible H<sub>2</sub>S capture in MOFs and (ii) chemical transformation of H<sub>2</sub>S within the pores of MOFs: formation of polysulphides.

**(i) High and reversible H<sub>2</sub>S capture in MOFs.** The capture of H<sub>2</sub>S by MOFs has confirmed some crucial difficulties such as the formation of strong bonds, typically irreversible, (*e.g.*, a metal–sulphur bond), which can compromise the chemical stability and cyclability of MOFs. Therefore, it is required to modulate host–guest interactions between the MOFs and H<sub>2</sub>S to avoid structure collapse and afford a feasible cyclability. In order to achieve these goals, such interactions should arise through noncovalent bonding between the functionalisation of MOFs and H<sub>2</sub>S guest molecules. For example, hydrogen bonding has been postulated, by density functional theory (DFT) methods and grand canonical Monte Carlo (GCMC) simulations,<sup>66</sup> as a promising moderate interaction between MOFs and H<sub>2</sub>S molecules. Experimentally, a remarkable work by Hamon and co-workers showed the high chemical stability and cyclability of MIL-47 (M = V<sup>4+</sup>) and MIL-53(M) (M = Al<sup>3+</sup>, Cr<sup>3+</sup>) when exposed to H<sub>2</sub>S.<sup>67</sup> These MOF materials are constructed with  $\mu$ -OH functional groups which presumably established hydrogen bonds with H<sub>2</sub>S.

Humphrey and Maurin showed the H<sub>2</sub>S capture on Mg-CUK-1.<sup>68</sup> This MOF is assembled from a 2,4-pyridinedicarboxylate

ligand and Mg<sup>2+</sup> octahedral centres, connected into infinite chains of [Mg<sub>3</sub>( $\mu_3$ -OH)]<sup>5+</sup> clusters by  $\mu_3$ -OH groups. Although the total H<sub>2</sub>S capture of Mg-CUK-1 was relatively low (3.1 mmol g<sup>−1</sup>), this material demonstrated to be chemically stable to H<sub>2</sub>S and a remarkably easy regeneration after the H<sub>2</sub>S capture using temperature swing re-activation (TSR). Most importantly, GCMC simulations showed how H<sub>2</sub>S molecules interact with the hydroxo functional groups (by moderate hydrogen bonds  $\mu_3$ -O–H...SH<sub>2</sub>), see Fig. 9.<sup>68</sup> Such moderate H<sub>2</sub>S/Mg-CUK-1 interaction was found to be consistent with easy regeneration of the material after H<sub>2</sub>S exposure.

This work demonstrated experimentally and in good correlation with advanced computational calculations, the chemical structure integrity of a hydroxo-functionalised MOF material to H<sub>2</sub>S, and the critical role of a moderate interaction (hydrogen bonding) to facilitate its cyclability. The study of more  $\mu$ -OH functionalised MOFs for the efficient and cyclable capture of H<sub>2</sub>S initiated.

Maurin and Gutiérrez-Alejandre investigated another  $\mu$ -OH functionalised MOF (MIL-53(Al)-TDC) for the capture of H<sub>2</sub>S.<sup>69</sup> This material, an Al<sup>3+</sup>-based constructed with a carboxylate ligand (TDC = 2,5-thiophenedicarboxylate) which contains [AlO<sub>4</sub>-*trans*-( $\mu$ -OH)<sub>2</sub>] octahedra where the Al<sup>3+</sup> centre coordinates to two  $\mu$ -OH groups and six oxygen atoms from the TDC ligands, has established the highest H<sub>2</sub>S adsorption (18.1 mmol g<sup>−1</sup> at room temperature) reported for a microporous material.<sup>69</sup> Structural stability of MIL-53(Al)-TDC, after the H<sub>2</sub>S capture experiment was corroborated by PXRD and SEM analyses. TGA experiments demonstrated the complete desorption of H<sub>2</sub>S molecules at 65 °C. H<sub>2</sub>S sorption–desorption cycles (five cycles with a value of 18.5 ± 0.7 mmol g<sup>−1</sup>) demonstrated high H<sub>2</sub>S regeneration capacity. This cyclability confirmed the full regeneration of the material by only increasing the temperature to 65 °C, showing the low energy requirement to fully desorb H<sub>2</sub>S. This suitable cyclability indicated weak interactions between H<sub>2</sub>S molecules and the pores of the material. *In situ* DRIFT experiments investigated the interactions between H<sub>2</sub>S and MIL-53(Al)-TDC, showing (i) the formation of hydrogen bonds between H<sub>2</sub>S molecules themselves confined in the pores of MIL-53(Al)-TDC; (ii) relatively weak interaction between H<sub>2</sub>S and the  $\mu$ -OH groups and (iii) H<sub>2</sub>S molecules interact with the



Fig. 9 H<sub>2</sub>S adsorption preferred site of magnesium-based CUK-1 material. And after confinement of 2.8% EtOH (red isotherm). Reprinted (adapted) with permission from ref. 68. Published (2018) by The Royal Society of Chemistry.







Fig. 10 Illustrative arrangements of  $\text{H}_2\text{S}$  in the pores of MIL-53-TDC generated from the GCMC simulations at (a)  $0.5 \text{ mmol g}^{-1}$  and (b)  $18.5 \text{ mmol g}^{-1}$ . The distances are reported in Å. (Al, pink; O, red; S, yellow; C, grey; H, white). Reprinted (adapted) with permission from ref. 69. Published (2019) by The Royal Society of Chemistry.

other functionality of the MOF: the thiophene ring from the TDC ligand.<sup>69</sup> To corroborate these interpretations from the DRIFT experiments, Monte Carlo simulations were carried out for different loadings corresponding to the experimental discoveries. These calculations corroborated that at low loading,  $\text{H}_2\text{S}$  interacts *via* its S-atom with the H-atom of the  $\mu\text{-OH}$  group (see Fig. 10), representing the preferential adsorption site. In addition, it was shown that  $\text{H}_2\text{S}$  also interacts with the thiophene ligand, and, upon increasing the  $\text{H}_2\text{S}$  loading, hydrogen bonds between the  $\text{H}_2\text{S}$  molecules were also identified (Fig. 10).<sup>69</sup>

These theoretical findings revealed the fundamental role of the thiophene ligand. Experimentally speaking, this M-OH hydroxo group containing functional material shows an extraordinarily facile re-activation leading to an easy  $\text{H}_2\text{S}$  cyclability, which should not be anticipated due to the dominant interaction between the  $\mu\text{-OH}$  group and  $\text{H}_2\text{S}$  reinforced further by the interaction of the  $\text{H}_2\text{S}$  molecule with the thiophene unit as demonstrated by *in situ* DRIFT measurements. However, computational calculations postulate that the interaction of  $\text{H}_2\text{S}$  with the thiophene ring weakens the interaction with the preferential adsorption site ( $\mu\text{-OH}$  group), favouring the easy displacement of the  $\text{H}_2\text{S}$  molecule when the material is re-activated.

As previously discussed, (*vide supra*) for the MFM-300(M) family, the extraordinary chemical stability arises from the strength of the coordination bonds between the oxygen atoms form the carboxylic ligand and the  $\text{M}^{3+}$  metal centres. Thus, MIL-53(Al)-TDC is very similar to MFM-300(Al) since it is also constructed with  $\text{Al}^{3+}$ . Therefore, the chemical stability of MIL-53(Al)-TDC towards  $\text{H}_2\text{S}$  is envisaged based on the same arguments used for MFM-300(Al).

**(ii) Chemical transformation of  $\text{H}_2\text{S}$  within the pores of MOFs: formation of polysulphides.** As described in the previous section, the study of more hydroxo-functionalised MOF materials attracted high interest since the promising results on the effective and efficient cyclable capture of  $\text{H}_2\text{S}$ . Thus, a couple of materials from the MFM-300(M) family were investigated by Maurin and Gutiérrez-Alejandre,<sup>70</sup> for the capture of  $\text{H}_2\text{S}$ : MFM-300(Sc) and MFM-300(In).

First, MFM-300(Sc) exhibited a  $\text{H}_2\text{S}$  uptake of  $16.5 \text{ mmol g}^{-1}$  (at  $25^\circ\text{C}$ ), which is comparable to the  $\text{H}_2\text{S}$  uptake of MIL-53(Al)-TDC ( $18.1 \text{ mmol g}^{-1}$ ).<sup>69</sup> Upon an inspection of the structural integrity of the material after the  $\text{H}_2\text{S}$  experiment, PXRD experiments revealed the retention of the crystalline structure. Interestingly, when investigating the porosity of MFM-300(Sc) after the  $\text{H}_2\text{S}$  uptake experiment, the pore volume was reduced by 34% from  $0.56$  to  $0.37 \text{ cm}^3 \text{ g}^{-1}$  indicating that some remaining species are still present in the pores of the material. After confirming the retention of the crystallinity and a reduction of the intrinsic porosity of MFM-300(Sc) after the first  $\text{H}_2\text{S}$  cycle, additional  $\text{H}_2\text{S}$  cycling experiments were performed. Over the second cycle, the  $\text{H}_2\text{S}$  adsorption capacity decreased by 39% to  $10.08 \text{ mmol g}^{-1}$ , which is in a good agreement with the reduction of the pore volume by about 34%. The average  $\text{H}_2\text{S}$  capture in cycles 2 to 5 was  $10.22 \text{ mmol g}^{-1}$ . After the fifth cycle, PXRD experiments corroborated the retention of the crystalline structure of MFM-300(Sc), while a  $\text{N}_2$  adsorption experiment showed that the pore retained its reduced volume of  $0.37 \text{ cm}^3 \text{ g}^{-1}$ . In an attempt to remove the remaining sulphur species formed inside the pores of MFM-300(Sc), the sample after the first  $\text{H}_2\text{S}$  cycle was activated at  $250^\circ\text{C}$ . After this thermal treatment, the pore volume did not change ( $0.37 \text{ cm}^3 \text{ g}^{-1}$ ) confirming that the sulphur species were irreversibly adsorbed within the MFM-300(Sc) framework.<sup>70</sup>

The identification of these sulphur species was first approached by TGA and diffuse-reflectance infrared Fourier-transform spectroscopy (DRIFT) experiments which corroborated strong interactions between the guest species and the pore-walls of MFM-300(Sc). Raman spectroscopy, complemented with elemental analysis (EDX) and conventional elemental analysis, postulated the first indication of the possible nature of the remaining (irreversibly adsorbed) sulphur species within the pores, *i.e.*, polysulphides (see Fig. 11).<sup>70</sup> Even though the redox properties of polysulphides are highly complex, electrochemical experiments were the key to fully identify them. An electrochemical cell (MFM-300(Sc))-CSP/PVDF/1 M LiTFSI in triglyme/Li0 (PVDF = poly(vinylidene difluoride), LiTFSI =  $\text{LiN}[\text{SO}_2\text{CF}_3]_2$ , triglyme =  $\text{MeO}[\text{CH}_2\text{CH}_2\text{-O}]_3\text{Me}$ ) was examined (for 20 h) through open-circuit potential (OCP) measurements and analysed by cyclic voltammetry. Then, this electrochemical cell showed an initial potential of  $2.29 \text{ V}$  (*vs.*  $\text{Li}^0/\text{Li}^+$ ) for MFM-300(Sc) and after reaching equilibrium, this potential was equal to  $2.15 \text{ V}$  (*vs.*  $\text{Li}^0/\text{Li}^+$ ).

Later, a  $\text{H}_2\text{S}$  exposed sample of MFM-300(Sc) ( $\text{H}_2\text{S}@ \text{MFM-300(Sc)}$ ) was used to construct a different electrochemical cell showing a different behaviour on the variation of the potentials (the potential increased from  $1.90$  to  $2.33 \text{ V}$  (*vs.*  $\text{Li}^0/\text{Li}^+$ )). According to Mikhaylik and Akridge,<sup>71</sup> electrochemical potentials lower than  $2.10 \text{ V}$  correspond to low-order polysulphides ( $\text{S}_n^{2-}$ , ( $n = 2$ )). Thus, the initial potential for  $\text{H}_2\text{S}@ \text{MFM-300(Sc)}$  of  $1.90 \text{ V}$  suggested the formation of such low-order  $\text{S}_2^{2-}$  polysulphides. The formation of these low-order species arises from the strong mutual  $\text{H}_2\text{S} \cdots \text{H}_2\text{S}$  hydrogen bond interactions with a characteristic  $\text{H}(\text{H}_2\text{S}) \cdots \text{S}(\text{H}_2\text{S})$  distance of  $2.91 \text{ Å}$ , as demonstrated in the corresponding RDF plot from the Monte Carlo simulations.



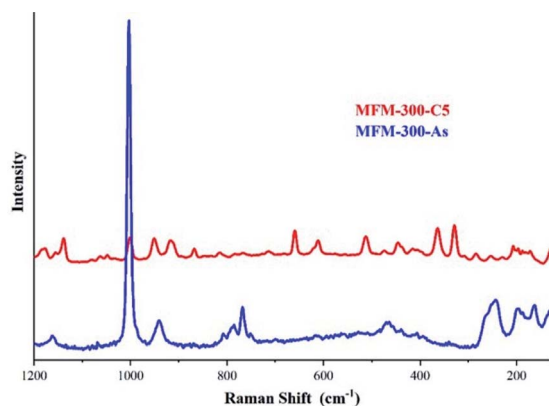


Fig. 11 Raman spectra of MFM-300(Sc) after 5 cycles of H<sub>2</sub>S (red) and as synthesised (blue). The peaks observed in the 350–520 cm<sup>−1</sup> region are associated to the S–S stretching vibrations modes of several polysulphides with various chain lengths. Reprinted with permission from ref. 70. Copyright (2020) American Chemical Society.

In the case of MFM-300(In) by constructing the equivalent electrochemical cell (MFM-300(In))–CSP/PVDF/1 M LiTFSI in triglyme/Li<sup>0</sup> and same operation conditions (OCP measurements and analysed by cyclic voltammetry for 20 h), the electrochemical cell exhibited an initial potential of 2.65 V (vs. Li<sup>0</sup>/Li<sup>+</sup>) for MFM-300(In) and after reaching equilibrium, this potential was equal to 2.15 V (vs. Li<sup>0</sup>/Li<sup>+</sup>). The difference of 0.36 V, from the initial potentials for MFM-300(Sc) and MFM-300(In), was attributed to the difference in the electronegativity of the metal centres (Sc<sup>3+</sup> and In<sup>3+</sup>) in both materials. After the adsorption of H<sub>2</sub>S, H<sub>2</sub>S@MFM-300(In), MFM-300(In) showed a different trend than MFM-300(Sc): the potential decreased from 2.50 to 2.15 V (vs. Li<sup>0</sup>/Li<sup>+</sup>). Such a trend difference for both stabilisation potentials and the potential values indicated that the chemical composition of the sulphur species in both materials (MFM-300(Sc) and MFM-300(In)) were different. Again, Mikhaylik and Akridge indicate,<sup>71</sup> that electrochemical potentials higher than 2.10 V correspond to high-order polysulphides (S<sub>n</sub><sup>2−</sup>), (*n* = 6). Such large polysulphides block completely the pores of MFM-300(In), as corroborated by the loss of the pore volume in H<sub>2</sub>S@MFM-300(In) (0.02 cm<sup>3</sup> g<sup>−1</sup>) and Raman spectroscopy. Interestingly, although these two materials are isostructural, a small difference in the pore size (8.1 and 7.5 Å for MFM-300(Sc) and MFM-300(In), respectively) contributes along with the different electrochemical potential of both materials (different electron densities) to the formation of distinct polysulphide species.

Although there is a hypothesis that justifies the polysulphide formation in both materials (based on the “disproportionation” type reaction,<sup>72</sup> were the protons of H<sub>2</sub>S play the role of an oxidant and the sulphide plays the role of a reducing agent), there is a great opportunity to deeply investigate this phenomenon. For example, can the polysulphide formation be a consequence of reversible metal–ligand bonding upon the adsorption of H<sub>2</sub>S? Recently Brozek and co-workers<sup>73</sup> elegantly demonstrated metal–ligand dynamics for carboxylate benchmark MOFs, *via* variable-temperature diffuse reflectance infrared

Fourier transform spectroscopy (VT-DRIFTS) coupled with *ab initio* plane wave density functional theory. Thus, new exciting horizons can be discovered by taking a different approach when H<sub>2</sub>S is adsorbed in MFM-300(M), which could explain such fascinating polysulphide formation.

The last MOF material, to date, that demonstrated the chemical transformation of H<sub>2</sub>S to polysulphides is SU-101.<sup>74</sup>

This bioinspired material was synthesised (by Inge *et al.*<sup>74</sup>), using ellagic acid, a common natural antioxidant, and bismuth (Bi<sub>2</sub>O(H<sub>2</sub>O)<sub>2</sub>(C<sub>14</sub>H<sub>2</sub>O<sub>8</sub>)·*n*H<sub>2</sub>O), see Fig. 12. Then, the resultant breakthrough H<sub>2</sub>S experiment led to a gas uptake of 15.95 mmol g<sup>−1</sup>, representing one of the highest H<sub>2</sub>S uptakes reported and even more interesting since the BET surface area of SU-101 (412 m<sup>2</sup> g<sup>−1</sup>) is considerably lower than top H<sub>2</sub>S capture materials (*e.g.*, MIL-53(Al)-TDC; BET = 1150 m<sup>2</sup> g<sup>−1</sup>). On a second H<sub>2</sub>S adsorption cycle, the initially observed capacity and surface area were reduced to only 0.2 mmol g<sup>−1</sup> and 15 m<sup>2</sup> g<sup>−1</sup>, respectively, even though the crystallinity was retained as confirmed by PXRD. Raman spectra of SU-101 (before and after H<sub>2</sub>S adsorption) confirmed the presence of low-order polysulphides (*n* = 2), S<sub>4</sub><sup>2−</sup>. Thus, the electrochemical potential of SU-101 should be similar to the one for MFM-300(Sc) (2.29 V),<sup>70</sup> considering that S<sub>4</sub><sup>2−</sup> species were only found for MFM-300(Sc). Future investigations are anticipated to continue in order to verify the electrochemical potential of SU-101 and any possible reversible metal–ligand bonding upon the adsorption of H<sub>2</sub>S.

A variety of MOFs, as well as classic materials such as zeolites, activated carbon and metal oxides, have been studied for the adsorption of these toxic gases, where some of these are summarized in Table 3. Noteworthy, the comparison of materials for H<sub>2</sub>S capture is sometimes challenging due to the difference in the experimental conditions (*e.g.*, flue gas concentration).

### 3.2 Bio-compatible MOFs for H<sub>2</sub>S detection and controlled delivery

Although H<sub>2</sub>S is catalogued as highly toxic, paradoxically, it can also be crucial as an endogenous biological mediator.<sup>82</sup>



Fig. 12 (a) The coordination environment around Bi<sup>3+</sup>. The bond to a coordinated water molecule is represented as a dashed line. (b and c) Chelation of ellagite ligand toward the bismuth oxo rods. Reprinted (adapted) with permission from ref. 74. Copyright (2020) American Chemical Society.



Table 3 Summary of the adsorption capacity of H<sub>2</sub>S for selected metal–organic frameworks and benchmark materials

MOF	BET Surface area [m <sup>2</sup> g <sup>−1</sup> ]	H <sub>2</sub> S adsorption [mmol g <sup>−1</sup> ]	Ref.
MIL-47(V)	930	14.6	67
MIL-53(Cr)	1946	12.0	67
MIL-53(Al)-BDC	1103	11.7	67
Ni-CPO-27	1547	12.0	85
Mg-CUK-1	604	3.1 <sup>a</sup>	68
MIL-53(Al)-TDC	1150	18.5	69
MIL-100(Fe)	2000	16.7	67
MIL-101(Cr)	2916	30.1	34
MIL-101(Cr)-4F(2%)	2176	36.9	34
MFM-300(Sc)	1350	16.5	70
Cu-BTC	1590	1.1	63
SU-101	412	15.95	74
PAF-302	5600	51.94	75
COF-102	3621	35.57 <sup>b</sup>	75
HKUST-1 <sup>c</sup>	—	2.7 <sup>d</sup>	60
10Mn-45Zn-45Ti-O <sup>e</sup>	—	0.0005	76
4A molecular sieve zeolite	49.5	0.0002 <sup>f</sup>	77
13X zeolite	440	0.007 <sup>g</sup>	78
SBA-15	950	1.98 <sup>h</sup>	79
PEI(50)/SBA-15(MBS-2)	80	0.0002 <sup>h</sup>	80
Wood-based AC	1400	0.008	81

<sup>a</sup> 15% vol H<sub>2</sub>S. <sup>b</sup> GCMC simulations. <sup>c</sup> Graphite-oxide composite. <sup>d</sup> 1000 ppm H<sub>2</sub>S in moist air. <sup>e</sup> H<sub>2</sub>S/H<sub>2</sub>/CO<sub>2</sub>/H<sub>2</sub>O (600 ppm : 25% : 7.5% : 1%). <sup>f</sup> 10% vol H<sub>2</sub>S. <sup>g</sup> 80 ppmv H<sub>2</sub>S. <sup>h</sup> 4000 ppmv of H<sub>2</sub>S and 20 vol% of H<sub>2</sub> in N<sub>2</sub>.

Endogenous pathways for H<sub>2</sub>S have been found to have wide extending activities *in vivo*, such as in the cardiovascular system.<sup>83</sup> For example, H<sub>2</sub>S executes a crucial activity in the regulation of blood pressure, neurotransmission, anti-inflammatory mechanism, anti-oxidation, angiogenesis and apoptosis.<sup>84</sup> H<sub>2</sub>S can be biosynthesised by enzymatic reactions *via* a sequence of endogenous processes,<sup>85</sup> and in the biological medium, the H<sub>2</sub>S concentration can fluctuate from nano-to micromolar levels.<sup>86</sup> However, at higher concentrations of H<sub>2</sub>S in the bloodstream can cause severe physiological disorders such as diabetes, Alzheimer's disease, cirrhosis, different types of cancer and Down's syndrome.<sup>87</sup>

Therefore, in order to recognise the specific role of H<sub>2</sub>S in these processes, the detection (spatial and temporal information) of H<sub>2</sub>S levels in living cells and organisms is crucial. However, due to the high reactivity, volatility and diffusible properties of H<sub>2</sub>S, traditional detection technologies (chromatography, high performance liquid chromatography, electrochemical analysis and colorimetric)<sup>88</sup> are unsuitable for the identification of H<sub>2</sub>S in living cells because they result in destruction of the cells and tissues and difficulties associated to real-time detection.<sup>89</sup> Fluorometric detection techniques have emerged as highly significant alternatives since their non-destructive characteristics, fast response, high selectivity and sensitivity, fast response, high spatial sampling capability, real-time monitoring and easy sample preparation.<sup>90</sup> Turn-on type fluorescence probes for H<sub>2</sub>S detection have been recently investigated and these are commonly based on the reactivity characteristics of H<sub>2</sub>S (*e.g.*, copper sulphide precipitation, dual nucleophilic addition, H<sub>2</sub>S-mediated hydroxyl amide and nitro/azide reduction).<sup>91</sup> Such characteristic reactivity of H<sub>2</sub>S can

efficiently distinguish it from other biological species; however, many of these detectors do not fulfil basic requirements such as rapid detection and selectivity. Thus, the investigation of new H<sub>2</sub>S probes is still very attractive due of the complexity of different molecular events involved in signalling transduction, and other complications related to the probes. Therefore, bio-compatible MOFs have been postulated as promising probes for the detection of H<sub>2</sub>S.

The first concept of a MOF material in *in vitro* H<sub>2</sub>S delivery was demonstrated by Morris and co-workers who used CPO-27 for this purpose.<sup>92</sup> H<sub>2</sub>S can be released by exposing the material to H<sub>2</sub>O since CPO-27 is an open metal site system thus, the water molecule replaces the hydrogen sulphide molecule at the metal site. The authors analysed the H<sub>2</sub>S delivery in two iso-structural materials (Zn-CPO-27 and Ni-CPO-27) finding that the Ni<sup>2+</sup> material exhibited higher delivery capacity than the Zn<sup>2+</sup> material: after 30 min 1.8 mmol g<sup>−1</sup> of H<sub>2</sub>S was released from Ni-CPO and only 0.5 mmol g<sup>−1</sup> from the Zn-CPO. After 1 h, the H<sub>2</sub>S release for both materials was completed. The amount of H<sub>2</sub>S released by each material corresponds to approximately 30% of the chemisorbed gas. Later, the release of H<sub>2</sub>S (stored in Zn-CPO-27 and Ni-CPO-27) was investigated under physiological conditions (endothelium-intact ring of pig coronary artery), finding a substantial vasodilatory action (relaxation) with only a short induction period of approximately 5 min.<sup>92</sup> These results represented a very significant progress in the field of MOFs and biological applications, since such H<sub>2</sub>S release mechanisms offered new protocols to better understand the effects of H<sub>2</sub>S on this particular vascular system.

Later, the first fluorescence probe example based on a MOF for the detection of H<sub>2</sub>S was presented by Wang and co-







Fig. 13 (a, b) Bright field image and fluorescence image after treating the HeLa cells with MN-ZIF-90 ( $0.05 \text{ mg mL}^{-1}$ ) after 48 h of incubation. (c) *In vitro* HeLa cell viabilities after 48 h of incubation with MN-IM and MN-ZIF-90 at different concentrations. Reprinted with permission from ref. 93. Copyright (2014) Springer Nature.

workers.<sup>93</sup> Through a post-synthetic modification of ZIF-90 with malononitrile ( $\text{N}\equiv\text{C}-\text{CH}_2-\text{C}\equiv\text{N}$ ), they obtained MN-ZIF-90 which undergoes a specific reaction with  $\text{H}_2\text{S}$ , achieving an enhancement of photoluminescence, constituting the base for the detection of  $\text{H}_2\text{S}$  (see Fig. 13). Then, the malononitrile moieties conjugated to the host (ZIF-90) through double bonds aided as quenchers of the host fluorescence through intramolecular photoinduced electron transfer. The detection mechanism was based on the  $\alpha,\beta$ -unsaturated bond of the malononitrile which is susceptible to thiol compounds, leading to the breaking of the double bond and thus, the fluorescence of MN-ZIF-90 was recovered once  $\text{H}_2\text{S}$  was introduced into the system. In addition, the probe exhibited favourable biocompatibility.<sup>93</sup>

Taking a different approach but keeping the fundamental idea of introducing a reactive site for  $\text{H}_2\text{S}$ , Tang *et al.*,<sup>94</sup> demonstrated the use of a porphyrin-based MOF for the fluorescent detection of  $\text{H}_2\text{S}$ . By introducing reactive  $\text{Cu}^{2+}$  metal centres into a  $\text{Al}^{3+}$  MOF material  $\{\text{CuL}[\text{AlOH}]_2\}_n$  ( $\text{H}_6\text{L}$  = mesotetrakis(4-carboxylphenyl) porphyrin) the detection of  $\text{H}_2\text{S}$  was selectively followed by fluorescence under physiological pH (see Fig. 14). Additionally, they successfully demonstrated the capability of the probe to detect exogenous  $\text{H}_2\text{S}$  in living cells, while the probe showed low toxicity and high biocompatibility.<sup>94</sup>

Later, Biswas and co-workers demonstrated, on a dinitro-functionalised UiO-66 ( $\text{UiO-66}-(\text{NO}_2)_2$ ), fluorescence turn-on behaviour towards  $\text{H}_2\text{S}$  in simulated biological medium (HEPES buffer, pH = 7.4).<sup>95</sup> Remarkably,  $\text{UiO-66}-(\text{NO}_2)_2$  exhibited highly sensitive fluorometric  $\text{H}_2\text{S}$  sensing while also showing a visually detectable colorimetric change to  $\text{H}_2\text{S}$  in daylight (see Fig. 15). In addition, the high selectivity of this functionalised MOF material to  $\text{H}_2\text{S}$  was preserved even when several other biological species were present in the detecting medium. Finally, fluorescence microscopy studies on J774A.1 cells demonstrated the effectiveness of  $\text{UiO-66}-(\text{NO}_2)_2$  for  $\text{H}_2\text{S}$  imaging in living cells, detection of  $\text{H}_2\text{S}$  in human blood plasma (HBP) and monitoring of the sulphide concentration in real water samples.<sup>95</sup> These results emphasised the biocompatibility



Fig. 14 Fluorescence spectra of porphyrin ligand ( $10 \mu\text{M}$ ) in BBS buffer (pH = 7.40, 20 mM) after titration with  $\text{HS}^-$  from 0–100  $\mu\text{M}$ ,  $\lambda_{\text{ex}} = 419$ . Reprinted with permission from ref. 94. Copyright (2014) American Chemical Society.

of  $\text{UiO-66}-(\text{NO}_2)_2$ . The reaction mechanism of  $\text{UiO-66}-(\text{NO}_2)_2$  and  $\text{H}_2\text{S}$  is caused by the reduction of the nitro groups to electron donating amine groups causing an increase in the fluorescence intensity that can be registered.

$\text{Eu}^{3+}/\text{Ag}^+/\text{UiO-66}-(\text{COOH})_2$  (EAUC) composites were reported by Li and Qian as biomarkers for the potential diagnosis of asthma.<sup>96</sup> The decrease of the  $\text{H}_2\text{S}$  production in the lung has been identified as an early detection biomarker for asthma. Thus, fluorescent experiments showed that EAUC exhibited high selectivity and sensitivity with a limit of a real-time  $\text{H}_2\text{S}$  detection of 23.53  $\mu\text{M}$ . The detection of  $\text{H}_2\text{S}$  by EAUC was based on the introduction of active metal centre ( $\text{Ag}^+$ ,  $\text{H}_2\text{S}$ -responding site) to the  $\text{Eu}^{3+}/\text{UiO-66}-(\text{COOH})_2$  as the lanthanide-luminescence sensitizer.<sup>96</sup> MTT assay and cell viability analysis in PC12 cells demonstrated relatively low cytotoxicity for EAUC and biocompatibility. Finally, the determination of  $\text{H}_2\text{S}$  was tested in diluted fetal bovine and human serum samples demonstrating that EAUC can detect  $\text{H}_2\text{S}$  in real biological samples. Zhang and co-workers<sup>97</sup> covalently modified (*via* click chemistry) PCN-58 with target-responsive two-photon (TP) organic moieties to fluorescently detect  $\text{H}_2\text{S}$ . These TP-MOF probes showed good photostability, high selectivity, minor cytotoxicity, and excellent  $\text{H}_2\text{S}$  sensing performance in live cells. These modified PCN-58 materials also showed intracellular sensing and depth imaging capabilities (penetration depths up to 130  $\mu\text{m}$ ).<sup>97</sup>



Fig. 15 Colorimetric detection behaviour of the HEPES suspension of  $\text{UiO-66}-(\text{NO}_2)_2$  with increasing concentration of  $\text{Na}_2\text{S}$  in daylight. Reprinted with permission from ref. 95. Published (2018) by The Royal Society of Chemistry.



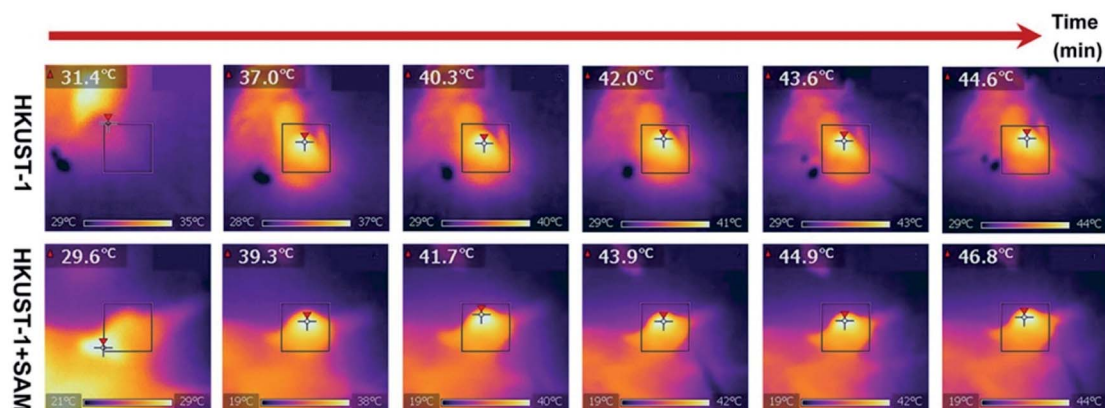


Fig. 16 *In vivo* antitumour efficacy of HKUST-1. Photothermal images of the tumour site after 4 h of intratumoural injection of HKUST-1 and HKUST-1 + SAM exposure to laser irradiation (808 nm, 1 W cm<sup>-2</sup>) at the 2 min interval. Reprinted with permission from ref. 98. Copyright (2020) American Chemical Society.

Up to this point we have presented remarkable examples of MOF materials for the detection of H<sub>2</sub>S (biomarkers). All of these have been constructed with the fundamental principle of incorporating into these MOFs “the right chemical functionality” which can react with H<sub>2</sub>S. Remarkably, Wang and Xie<sup>98</sup> took a step forward and very recently showed how an endogenous MOF-biomarker-triggered “turn-on” strategy was capable to produce therapeutic agents *in situ*, as a promising example in nanomedicine for the precise treatment of colon cancer. HKUST-1 was used as an endogenous H<sub>2</sub>S-activated copper MOF which demonstrated to synergistically mediate H<sub>2</sub>S-activated near-infrared photothermal therapy and chemodynamic therapy. As a proof of principle, the protocol worked as follows: in normal tissues, the photoactivity of as-synthesised HKUST-1 nanoparticles was in the “OFF” state, and no obvious adsorption within the NIR region was observed. On the other hand, when HKUST-1 nanoparticles with high overexpression of H<sub>2</sub>S reached the colon tumour tissues, these nanoparticles were activated to the “ON” state by reacting with endogenous H<sub>2</sub>S to produce *in situ* photoactive copper sulphide with stronger NIR absorption, which is viable for the subsequent photothermal therapy and corresponding thermal imaging (see Fig. 16). In addition, besides the *in situ* formation of the photothermal agent, HKUST-1 nanoparticles also showed a horseradish peroxidase (HRP)-mimicking activity to efficiently convert overexpressed H<sub>2</sub>O<sub>2</sub> within cancer cells into more toxic ·OH radicals for chemodynamic therapy. Thus, this promising H<sub>2</sub>S-triggered “turn-on” strategy based on the endogenous biomarker from the tumour microenvironment can provide a precise diagnosis, marginal invasion, and possibly clinical translation.<sup>98</sup>

## 4. Ammonia

NH<sub>3</sub> is one of the most important chemicals in the world since it is an irreplaceable feedstock for global agriculture and industry (e.g., fertilizers, drug production, heat pumps and fuel cells).<sup>99</sup> Although fundamental to our diet supply and economy, NH<sub>3</sub> is a highly toxic (even in small concentrations) and corrosive gas (i.e., difficult to handle and store). Thus, considerably large

emissions of NH<sub>3</sub> from livestock breeding, industrial production, fertiliser application and public transportation can have serious consequences on the environment (highly unfavourable to air quality and aquatic life), and human health.<sup>100</sup> In addition, NH<sub>3</sub> reacts with NO<sub>x</sub> and SO<sub>2</sub> to form PM<sub>2.5</sub>, seriously contributing to the increase of air pollution.

NH<sub>3</sub> is a colourless gas with a characteristic pungent smell which is typically liquefied and confined in metal tanks in order to be efficiently stored and transported.<sup>101</sup> This implies high pressures (approximately 18 bar) and constant corrosion of pipelines and containers. Thus, new sorbent technologies capable of efficiently removing or storing NH<sub>3</sub> are highly desirable for air remediation and separation of NH<sub>3</sub> from N<sub>2</sub> and H<sub>2</sub> since NH<sub>3</sub> is considered an interesting energy intermediate.<sup>102</sup> It is clear that capture and recycling of NH<sub>3</sub> implies a dual connotation in the fields of environment and energy. Classic materials such as activated carbons, zeolites, silicas and even organic polymers have been investigated for the capture and separation of NH<sub>3</sub> showing low uptakes, poor selectivity and, in some cases, irreversible storages.<sup>103,104</sup> MOFs have been postulated as a promising option for NH<sub>3</sub> capture, due to the access to a wide range of chemical functionality (e.g., Lewis or Brønsted acid sites which provide higher affinity to the basic NH<sub>3</sub> molecule).<sup>104</sup> However, the main problem that most MOF materials exhibit poor chemical stability towards NH<sub>3</sub>.<sup>105</sup> The following section describes chemically stable MOFs with interesting NH<sub>3</sub> capture performances.

### 4.1 MOFs for NH<sub>3</sub> capture

The NH<sub>3</sub> molecule is a Lewis and Brønsted base which is the key to its adsorption on the porous surface of chemically stable MOFs. Thus, the incorporation of acidic functional groups within the MOFs is required to achieve relevant NH<sub>3</sub> capture results. These functionalisations can be organised in three main types: (i) coordinatively unsaturated metal sites (open metal sites), (ii) μ-OH groups and (iii) defective sites.

**(i) Coordinatively unsaturated metal sites.** The majority of MOF materials evaluated for the capture of NH<sub>3</sub> have demonstrated to be chemically unstable.<sup>106</sup> However, really interesting



examples have been reported by Dincă and co-workers.<sup>107</sup> They reported a series of new mesoporous MOFs constructed from extended bisbenzenetriazolate ligands and coordinatively unsaturated metal sites ( $\text{Mn}^{2+}$ ,  $\text{Co}^{2+}$ , and  $\text{Ni}^{2+}$ ), which showed high and reversible  $\text{NH}_3$  uptakes (15.47, 12.00, and 12.02  $\text{mmol g}^{-1}$ , respectively).<sup>107</sup> During desorption at different temperatures, all three materials showed pronounced hysteresis which emphasised the strong interaction between the open metal sites and  $\text{NH}_3$ . Such bound  $\text{NH}_3$  molecules can be fully removed upon heating the materials up to 200 °C under dynamic vacuum. Interestingly, none of the three materials showed a decrease in the  $\text{NH}_3$  uptake capacity upon cycling. Thus, the high chemical stability of azolate MOFs with open metal sites, towards  $\text{NH}_3$  postulate them as promising alternatives in environmental applications such as the capture of corrosive gases from power plant flue gas streams. This chemical stability can be attributed to the strength of the N atom coordinated to divalent metal centres as described previously.<sup>21</sup> In this case, the use of linear bistriazolate ligand, in combination with late transition metals such as  $\text{Ni}^{2+}$ , increases the heterolytic metal–ligand bond strength due to its higher basicity (compared to a carboxylate ligand) which allows better MOF stability to acidic gas exposure. This trend is also explained by Pearson's acid and base principle due to  $\text{Mn}^{2+}$ ,  $\text{Cu}^{2+}$  and  $\text{Ni}^{2+}$  are considered soft cations due to their charge/radius ratio, and nitrogen-based linkers are softer than carboxylate linkers.<sup>35</sup>

Later, the Dincă's group reported another series of microporous triazolate MOFs (containing open metal sites;  $\text{Cu}^{2+}$ ,  $\text{Co}^{2+}$ , and  $\text{Ni}^{2+}$ , see Fig. 17), that exhibited remarkable static and dynamic  $\text{NH}_3$  capacities (up to 19.79  $\text{mmol g}^{-1}$ , at 1 bar and 298 K).<sup>108</sup> These isorecticular analogues to the bisbenzenetriazolate examples,<sup>107</sup> are constructed from smaller triazolate ligands and therefore, they exhibited smaller pore windows (see Fig. 17). Interestingly, these microporous MOFs showed higher  $\text{NH}_3$  captures than their mesoporous analogues.<sup>107</sup> This remarkable property was not only accounted by the increase in the density

of open metal sites, in addition cooperative proximity effects resulted very important.  $\text{NH}_3$  breakthrough experiments on these microporous materials showed the potential applicability for both personal protection and gas separations ( $\text{NH}_3$  capacities of 8.56  $\text{mmol g}^{-1}$ ). Finally, once again, the superior chemical stability of these triazolate MOFs arises, as previously described, from the coordination of the N atom to metal centres (*vide supra*).

Very recently, Hong and co-workers recently presented the  $\text{NH}_3$  adsorption properties of  $\text{M}_2(\text{dobpdc})$  MOFs ( $\text{M} = \text{Mg}^{2+}$ ,  $\text{Mn}^{2+}$ ,  $\text{Co}^{2+}$ ,  $\text{Ni}^{2+}$ , and  $\text{Zn}^{2+}$ ;  $\text{dobpdc}^{4-} = 4,4\text{-dioxidobiphenyl-3,3-dicarboxylate}$ ), which after activation exhibited open metal sites (see Fig. 18).<sup>109</sup> The  $\text{NH}_3$  uptake of  $\text{Mg}_2(\text{dobpdc})$  at 298 K and 1 bar was 23.9  $\text{mmol g}^{-1}$  at 1 bar and 8.25  $\text{mmol g}^{-1}$  at 570 ppm, representing the  $\text{NH}_3$  record high capacities at both pressures among existing porous adsorbents.<sup>109</sup>  $\text{Mg}_2(\text{dobpdc})$  remarkably demonstrated chemical stability to not only dry  $\text{NH}_3$ , but also to wet  $\text{NH}_3$  ( $\text{NH}_3 \cdot \text{H}_2\text{O}$  vapour). Three consecutive  $\text{NH}_3$  sorption isotherms (activation included only application of vacuum) demonstrated the cyclability of  $\text{Mg}_2(\text{dobpdc})$ . To evaluate the affinity of the  $\text{NH}_3$  molecule to the open  $\text{Mg}^{2+}$  sites in  $\text{Mg}_2(\text{dobpdc})$ ,  $\text{NH}_3$ -TPD curves demonstrated (based on the Redhead analysis) the activation energy for  $\text{NH}_3$  desorption of 146.7  $\text{kJ mol}^{-1}$ . The  $\text{NH}_3$  adsorption mechanism of  $\text{Mg}_2(\text{dobpdc})$  was investigated by *in situ* FTIR experiments, indicating that  $\text{NH}_3$  was preferentially adsorbed, by coordination bonds, to the open metal sites of  $\text{Mg}_2(\text{dobpdc})$ . As the MOF sample was exposed to atmosphere the adsorbed  $\text{NH}_3$  in  $\text{Mg}_2(\text{dobpdc})$  was converted to  $\text{NH}_4^+$ , due to its reaction with atmospheric moisture. Dynamic  $\text{NH}_3$  breakthrough curves under dry conditions (0% relative humidity (RH) and 298 K) showed a  $\text{NH}_3$  capacity of 8.37  $\text{mmol g}^{-1}$  for  $\text{Mg}_2(\text{dobpdc})$ . When performing these  $\text{NH}_3$  breakthrough experiments under 80% RH conditions, the  $\text{NH}_3$  capacity of  $\text{Mg}_2(\text{dobpdc})$  decreased to 6.14  $\text{mmol g}^{-1}$ , due to the competitive adsorption between  $\text{NH}_3$  and  $\text{H}_2\text{O}$ . Additionally, this  $\text{NH}_3$  capacity remained



Fig. 17 Structure of  $\text{Co}_2\text{Cl}_2$  BTDD (left) and  $\text{Co}_2\text{Cl}_2$  BBTA (right). C, gray; O, red; N, blue; Cl, green; Co, purple. Hydrogen atoms have been omitted for clarity. Reprinted with permission from ref. 108. Copyright (2018) American Chemical Society.



Fig. 18 Atomic structure of  $\text{M}_2(\text{dobpdc})$  complexes with one-dimensional hexagonal channels. It is possible to observe that each coordinatively unsaturated metal site points towards the channel. Reprinted (adapted) with permission from ref. 109. Copyright (2020) John Wiley & Sons.





constant over five breakthrough wet cycles.<sup>109</sup> Thus,  $\text{Mg}_2(\text{-dobpdc})$  is an exceptional MOF material that can be easily synthesised (*i.e.*, microwave-assisted), highly recyclable (even after exposure to a humid  $\text{NH}_3$ ) without structural degradation or  $\text{NH}_3$  capacity loss and holds the record for the highest  $\text{NH}_3$  uptake at room temperature and atmospheric pressure.

All of these relevant properties are possible due to the exceptional chemical stability of this  $\text{Mg}^{2+}$ -based MOF material. But why is it so stable towards  $\text{NH}_3$ ? The authors proposed that such chemical stability was due to the higher affinity of  $\text{Mg}^{2+}$  to oxygen atoms than nitrogen atoms, as confirmed by van der Waals (vdW)-corrected density functional theory (DFT) calculations. They further investigated the origin of such remarkable chemical stability finding that the oxygen adjacent to the carboxylate participates in the coordination of the ligand to the  $\text{Mg}^{2+}$  cation acting as a tetratopic linker, similar to a chelate effect, increasing the stability of the cluster. This strategy is widely used to prevent pore collapse due to the activation energy barrier to ligand reorganisation or removal, which is increased by the higher linker connectivity.<sup>21</sup>

**(ii)  $\mu\text{-OH}$  groups.** The MFM-300(M) family (see the section of  $\text{SO}_2$ ) demonstrated remarkable  $\text{NH}_3$  adsorption properties with high uptakes and attractive cyclabilities. First, MFM-300(Al), reported by Yang and Schröder, showed a total  $\text{NH}_3$  capture of  $15.7 \text{ mmol g}^{-1}$  at 273 K and 1.0 bar.<sup>110</sup> Although the  $\text{NH}_3$  capture was not particularly high (even at a lower temperature than typically 298 K), the identification of the preferential  $\text{NH}_3$  adsorption sites was achieved by sophisticated *in situ* neutron powder diffraction (NPD) and synchrotron FTIR microspectroscopy. Thus, a structural analysis *via* Rietveld refinement of NPD data for 1.5  $\text{ND}_3$  (deuterated ammonia)/Al-loaded MFM-300(Al) identified three distinct binding sites (I, II and III) in  $[\text{Al}_2(\text{OH})_2(\text{L})](\text{ND}_3)_3$ , ( $\text{H}_4\text{L} = 1,1'$ -biphenyl-3,3',5,5'-tetracarboxylic acid =  $\text{C}_{16}\text{O}_8\text{H}_6$ ) (see Fig. 19). This cooperative network of  $\text{ND}_3$  molecules spreads down the length of the 1D channel, fixed in place by site I. Bond distances for sites II $\cdots$ III and a slightly lengthened site I $\cdots$ II are similar to a characteristic intermolecular bond between  $\text{ND}_3$  molecules in the solid state at very low temperature (*i.e.*, 2 K ( $\text{N}\cdots\text{D} = 2.357(2) \text{ \AA}$ )), while the

bond between the framework  $\mu_2\text{-OH}$  and site I is considerably shorter. Upon increasing the  $\text{ND}_3$  loading (from 0.5  $\text{ND}_3/\text{Al}$  to 1.5  $\text{ND}_3/\text{Al}$ ), a general shortening of the framework  $\mu_2\text{-OH}\cdots$ site I and sites I $\cdots$ II and an increase in the site II $\cdots$ III was observed.

Refinement of the NPD data for  $\text{ND}_3$ -loaded MFM-300(Al) demonstrated that on increasing the loading and thus the  $\text{ND}_3/\mu_2\text{-OH}$  ratio, the hydrogen atoms of the hydroxo functional groups experienced a reversible site exchange with the deuterium from the guest  $\text{ND}_3$  molecules residing at site I in the pore to resulting in the formation of  $\mu_2\text{-OD}$  moieties.<sup>110</sup> Interestingly, this H-D reversible exchange did not lead to any detectable structural degradation of the long-range order of the MOF material. Thus, the adsorption of  $\text{ND}_3$  in MFM-300(Al) showed a new type of adsorption mechanism where adsorbent and adsorbate experienced a rapid site-exchange *via* reversible formation and cleavage of O-H and O-D chemical bonds, in other words a pseudo-chemisorption binding mechanism.

Very recently, Yang and Schröder expanded the investigation on more MFM-300(M) ( $\text{M} = \text{Fe}^{2+}, \text{V}^{4+}, \text{Cr}^{3+}, \text{In}^{3+}$ ) materials and  $\text{NH}_3$ .<sup>111</sup> MFM-300(M) ( $\text{M} = \text{Fe}^{2+}, \text{V}^{3+}, \text{Cr}^{3+}$ ) demonstrated fully reversible  $\text{NH}_3$  capture for over 20 adsorption-desorption cycles, under pressure-swing conditions, reaching capacities of 16.1, 15.6, and  $14.0 \text{ mmol g}^{-1}$ , respectively, at 273 K and 1 bar. In the case of MFM-300(In), a significant loss of  $\text{NH}_3$  capture capacity over repeated  $\text{NH}_3$  cycles was shown which corroborated its chemical instability. On the other hand, MFM-300( $\text{V}^{4+}$ ) exhibited the highest  $\text{NH}_3$  uptake ( $17.3 \text{ mmol g}^{-1}$ ) among the MFM-300(M) family. Interestingly, the  $\text{NH}_3$  desorption phase for MFM-300( $\text{V}^{4+}$ ), with pore dimensions of approximately  $6.7 \times 6.7 \text{ \AA}^2$ , showed a hysteresis loop. Although this could indicate a characteristic capillary  $\text{NH}_3$  condensation (*e.g.*, in mesopores and/or due to a broad distribution of pore size and shape), the authors demonstrated, taking into account the pore dimensions of this MOF, a specific and potentially strong host-guest charge transfer upon the adsorption of  $\text{NH}_3$ . In addition, MFM-300( $\text{V}^{4+}$ ) showed an increase of both  $\text{NH}_3$  capacity and residue within the first 18 cycles, which was not observed for the rest of the MFM-300(M) materials. Such residual amount of  $\text{NH}_3$  left within MFM-300( $\text{V}^{4+}$ ) upon regeneration (pressure-swing) gradually increased from 8 to 20% along these cycles, indicating an increase of strongly bound NH-derived species in MFM-300( $\text{V}^{4+}$ ). This NH-derived residue, which was not desorbed by only reducing the pressure, was completely removed by increasing the temperature under dynamic vacuum, although some structural degradation of MFM-300( $\text{V}^{4+}$ ) was observed. The chemical stability of these materials to  $\text{NH}_3$  under humid conditions was investigated by PXRD, confirming the retention of their crystallinity for both MFM-300(M) ( $\text{M} = \text{Cr}^{3+}, \text{V}^{3+}$ ), while MFM-300(M) ( $\text{M} = \text{Fe}^{3+}, \text{V}^{4+}$ ) showed some structural degradation.<sup>111</sup>

Neutron powder diffraction data for  $\text{ND}_3$ -loaded MFM-300(M) combined with Rietveld refinements, showed the preferential binding sites for  $\text{ND}_3$  (Fig. 20). Two binding sites for  $\text{ND}_3$  were clearly identified for MFM-300(M) ( $\text{M} = \text{In}^{3+}, \text{V}^{3+}$ ), while MFM-300(Fe) has an additional binding site for  $\text{ND}_3$ . Site I showed the highest occupancy, with hydrogen bonding between the hydroxo functional group and the  $\text{ND}_3$  molecule ( $\mu_2\text{-OH}\cdots$

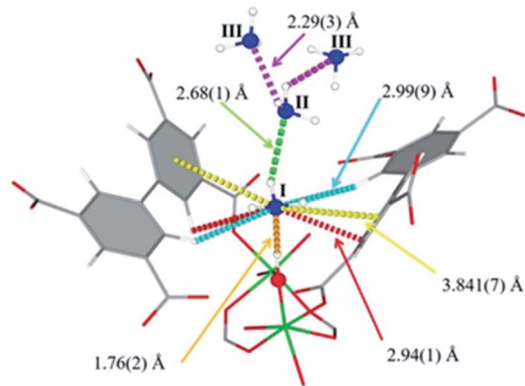


Fig. 19 Binding sites for  $\text{ND}_3$  molecules adsorbed within MFM-300(Al) determined by *in situ* NPD studies. Reprinted with permission from ref. 110. Copyright (2018) John Wiley & Sons.



ND<sub>3</sub>) (1.411–1.978 Å), complemented by additional hydrogen bonding from the organic ligand ( $H_{\text{aromatic}} \cdots \text{ND}_3 = 2.738\text{--}3.174$  Å;  $\text{ND}_3 \cdots \text{O}_{\text{ligand}} = 3.078\text{--}3.179$  Å) and electrostatic interactions ( $\text{ND}_3 \cdots \text{aromatic rings} = 2.946\text{--}3.132$  Å) (Fig. 20). Similar to MFM-300(Al),<sup>110</sup> hydrogen/deuterium site exchange was also observed between the adsorbed ND<sub>3</sub> and the  $\mu_2$ -OH group on for MFM-300(M) (M = In<sup>3+</sup>, Fe<sup>3+</sup>, V<sup>3+</sup>). Site II is located toward the centre of the pore (fixed by hydrogen-bonding interactions  $\text{ND}_3 \cdots \text{O}_{\text{ligand}} = 2.284\text{--}3.065$  Å). Site III in MFM-300(Fe) is constructed by electrostatic interactions ( $\text{ND}_3 \cdots \text{aromatic rings} = 3.146$  Å). Additionally, in MFM-300(Fe), intermolecular hydrogen bonds between ND<sub>3</sub> molecules (2.327 Å) were identified, propagating along the 1D channel to form a cooperative  $\{\text{ND}_3\}_\infty$  network.

The preferential ND<sub>3</sub> binding sites for MFM-300(V<sup>4+</sup>) were identified and these were different to the previous examples. MFM-300(V<sup>4+</sup>) is not constructed with  $\mu_2$ -OH groups. It shows bridging oxo centres to balance the charge of the oxidised V centre. Thus, ND<sub>3</sub> molecules are located in the centre of the pore. This particular arrangement implicates a very interesting situation: chemical reaction between the ND<sub>3</sub> molecules: a N<sub>2</sub>D<sub>4</sub> molecule was formed and located at site II with a ND<sub>3</sub> molecule at site I (being partially protonated to ND<sub>4</sub><sup>+</sup>). Then, both sites are stabilised *via* hydrogen bonding ( $\text{ND}_3 \cdots \text{O}_{\text{ligand}} = 2.529\text{--}3.092$  Å), and the amount of N<sub>2</sub>D<sub>4</sub> at site II was estimated as 0.5 N<sub>2</sub>H<sub>4</sub> per V centre.

The formation of N<sub>2</sub>H<sub>4</sub> was explained in terms of the redox activity of MFM-300(V<sup>4+</sup>) which promotes a host–guest charge transfer between the material and the adsorbed NH<sub>3</sub> molecules, promoting the reduction of the V<sup>4+</sup> centres and oxidation of NH<sub>3</sub> to N<sub>2</sub>H<sub>4</sub>.<sup>111</sup> These host–guest charge transfer results were

experimentally determined by EPR and corroborated by bond valence sum (BVS) calculations, finding as well that the charge transfer between adsorbed NH<sub>3</sub> molecules and the V<sup>4+</sup> centre can only occur when the loading of NH<sub>3</sub> is sufficiently high so that a predominant occupancy of the N site, which is located close to the metal chain, is reached to initiate the redox reaction. Finally, such mechanisms could also be investigated by the approach of metal–ligand dynamics as recently proposed by Brozek and co-workers,<sup>73</sup> to fully understand the interaction of NH<sub>3</sub> and the hydroxo functional group in the MFM-300(M) family.

**(iii) Defective sites.** As previously described in the SO<sub>2</sub> capture section (*vide supra*), crystal irregularities can provide very particular physical and chemical properties. Then, defects in MOF materials also demonstrated remarkable NH<sub>3</sub> adsorption properties. Very recently, Wu and Tsang presented a comprehensive study on the responsive adsorption behaviours of defect-rich Zr-based MOFs upon the progressive incorporation of NH<sub>3</sub>.<sup>112</sup> They investigated UiO-67 and UiO-bpydc containing 4,4'-biphenyl dicarboxylate and 4,4'-(2,2'-bipyridine) dicarboxylate ligands, that despite their structural similarities demonstrated a drastic difference in the NH<sub>3</sub> adsorption properties when the biphenyl groups in the organic ligand were replaced by the bipyridine moieties. Such replacement can confer flexibility to the framework in the context of mainly ligand “flipping” but without significant pore volume alteration.

Then, defective UiO-67 (non-monodisperse pore structure created by missing ligand defects) was synthesised thanks to the high connectivity of the Zr<sub>6</sub> oxoclusters, which help to retain the overall crystal structures even with some ligands are missing. UiO-67 involves uniform trigonal windows with a diameter of 11 Å that lead to interconnected tetrahedral and octahedral pores inside the structures. In the presence of missing ligand defects, the trigonal windows surrounding the defects in UiO-bpydc are fused into lozenge windows with a dynamic size larger than 14 Å. NH<sub>3</sub> adsorption–desorption isotherms at 298 K and up to 1 bar were performed for both materials: UiO-67 and UiO-bpydc. In the case of UiO-67, the adsorption isotherm showed “step-like shape” with two events (see Fig. 21, bottom). This characteristic isotherm shape is caused in MOFs by a gate-opening phenomenon due to the interaction between guest NH<sub>3</sub> molecules and pore walls, or a pore filling process.<sup>113</sup> Thus, at the beginning of the adsorption, the rapid and sudden increase in NH<sub>3</sub> adsorption at approximately 30 mbar (1.70 mmol g<sup>−1</sup>) (position I) suggests the presence of strong adsorption sites inside the framework, *e.g.*, strong interaction of the NH<sub>3</sub> molecules with the hydroxo ( $\mu_3$ -OH) functional groups. Later, the NH<sub>3</sub> uptake increased from 2.40 to 4.40 mmol g<sup>−1</sup> at 250 mbar (position II) and from 5.60 to 8.40 mmol g<sup>−1</sup> at 650 mbar (position III, Fig. 21). The desorption phase exhibited large, opened hysteresis, indicating that the NH<sub>3</sub> molecules strongly interact with the pore walls of the material.<sup>112</sup> These NH<sub>3</sub> molecules were fully desorbed by heating up to 423 K for 1 h under dynamic vacuum. Later, the chemical stability of UiO-67 towards NH<sub>3</sub> was investigated by conducting three NH<sub>3</sub> adsorption–desorption cycles and finally exposing the material to NH<sub>3</sub> vapour for 1 week. PXRD experiments corroborated the



Fig. 20 Preferential ND<sub>3</sub> binding sites in MFM-300(M) family (M = Cr, Fe, V<sup>3+</sup>, V<sup>4+</sup>) determined by NPD at 10 K. Views along *c* axis. Reprinted with permission from ref. 111. Copyright (2021) American Chemical Society.





Fig. 21 (Top) Refined ND<sub>3</sub> positions in the UiO-67 structure at ND<sub>3</sub> loadings of (a) 1.23, (b) 4.63, and (c) 7.60 mmol g<sup>-1</sup> obtained from NPD data at 300 K. ND<sub>3</sub> molecules at different binding sites: site I: yellow, site II: blue, site III: light blue, site IV: pink, and site V: green. (Bottom) NH<sub>3</sub> sorption isotherm at 298 K and up to 1100 mbar; adsorption: closed circles; desorption: open circles reprinted with permission from ref. 112. Copyright (2021) American Chemical Society.

stability of UiO-67 to dry and humid NH<sub>3</sub>. Then, in order to identify the preferential NH<sub>3</sub> adsorption sites in UiO-67, *in situ* high-resolution neutron powder diffraction (NPD) and synchrotron powder X-ray diffraction (SPXRD) experiments were carried out. The refined structures of UiO-67 at different ND<sub>3</sub> pressures, revealed five such adsorption preferential sites (Fig. 21).<sup>112</sup> At site I, the ND<sub>3</sub> was found close to the  $\mu_3$ -OH with a OH...N<sub>I</sub> distance of 1.96(1) Å, and O...N<sub>I</sub> distance of 2.80(1) Å (see Fig. 21). This distance suggested the formation of a relatively strong H-bonding interaction between the  $\mu_3$ -OH and ND<sub>3</sub>, similar to the one reported by Yang and Schröder in the MFM-300(M) family.<sup>110,111</sup> ND<sub>3</sub> molecules at site II were situated close to the walls of the trigonal windows suggesting interactions with the MOF organic ligands ( $H_{\text{ligand}} \cdots N_{\text{II}} = 2.58(1)$  and 2.68(1) Å), Fig. 21. On increasing the amount of ND<sub>3</sub>, these molecules were located near to the tetragonal pore (sites III and IV). At site III, the ND<sub>3</sub> molecule filled the shallow pore positions with N<sub>II</sub>...N<sub>III</sub> bond distances among these ND<sub>3</sub> sites in the range of 2.33(1) and 2.57(1) Å, creating a H-bonded network of these ND<sub>3</sub> molecules (Fig. 21).

In the case of UiO-bpydc, the NH<sub>3</sub> adsorption isotherm exhibited an uptake of 8.4 mmol g<sup>-1</sup> at 298 K and 1 bar (see Fig. 22). Conversely to UiO-67, UiO-bpydc showed only one large and sharper transition step (position II') for the NH<sub>3</sub> adsorption phase (Fig. 22). Then, *in situ* NPD experiments and followed by Rietveld refinements corroborated the existence of missing ligand defects. Similarly to UiO-67, the preferential NH<sub>3</sub> adsorption sites within UiO-bpydc were also identified by *in situ*

NPD experiments (replacing NH<sub>3</sub> by ND<sub>3</sub>). Thus, two independent preferential sites of ND<sub>3</sub> were found close to the  $\mu_3$ -OH functional group (site I') and to the organic ligands (site II', bipyridine ligand), Fig. 22. This strongly suggested that the adsorption of ND<sub>3</sub> mainly takes place at site II'. For site I', the OH...N<sub>I</sub> bond distance was estimated to be 2.10(2) Å, which is similar to that found in the isostructural UiO-67. Interestingly, the ND<sub>3</sub>-bipyridine ligand interaction was estimated to be stronger than the ND<sub>3</sub>-biphenyl ligand interaction with longer distances ( $H_{\text{ligand}} \cdots N_{\text{II}} = 2.68(1)$ , 3.19(1), and 3.20(1) Å, respectively) (see Fig. 22). Increasing the dosing of ND<sub>3</sub> molecules, increased the H-bonding between the ND<sub>3</sub> molecules giving rise to a network of six ND<sub>3</sub> molecules with the three bipyridine ligand located around the trigonal window. This particular situation demonstrated the gate-opening/closing behaviour *via* ligand flipping of UiO-bpydc upon ND<sub>3</sub> adsorption.<sup>112</sup>

This phenomenon was further investigated by DFT calculations to understand the role of the bipyridine ligands of UiO-bpydc in forming the H-bonding network with NH<sub>3</sub>

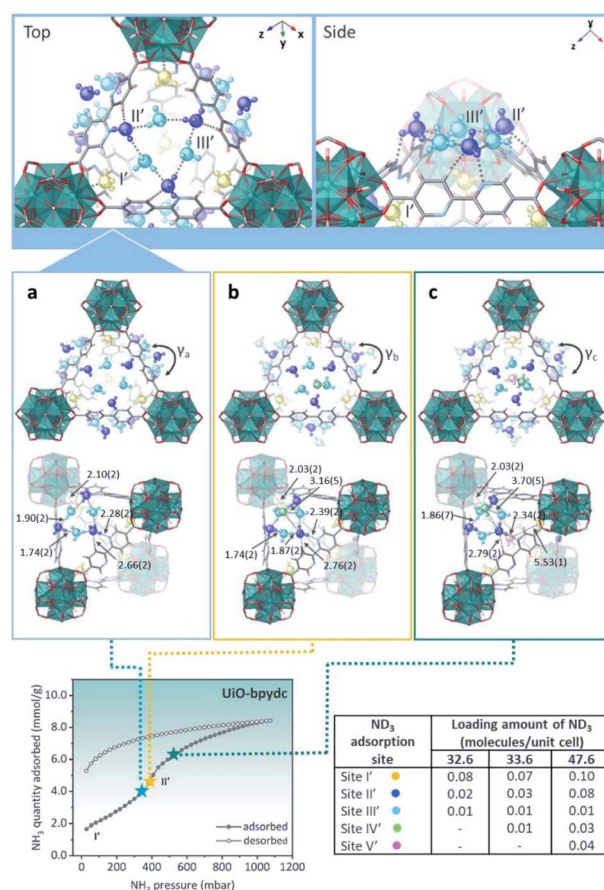


Fig. 22 (Top) Refined ND<sub>3</sub> positions in the UiO-bpydc structure at ND<sub>3</sub> loadings of (a) 4.15, (b) 4.27, and (c) 6.06 mmol g<sup>-1</sup> obtained from NPD data at 300 K. (Bottom) ND<sub>3</sub> molecules at different binding sites: site I': yellow, site II': blue, site III': light blue, site IV': green, and site V': pink. NH<sub>3</sub> sorption isotherm at 298 K and up to 1100 mbar; adsorption: closed circles; desorption: open circles reprinted with permission from ref. 112. Copyright (2021) American Chemical Society.



molecules, in comparison with the biphenyl ligands of UiO-67. Thus, the DFT-optimised structures demonstrated the progressive distortion of the aligned bipyridine ligands with  $\gamma$  changed from  $20.34^\circ$  (in good agreement with the NPD refined desolvated structure of UiO-bpydc) to  $19.47^\circ$ ,  $10.83^\circ$ ,  $9.49^\circ$ , and  $6.33^\circ$  by increasing the number of  $\text{NH}_3$  molecules at the trigonal window. Finally, these remarkable results demonstrated that the different pore openings (windows) induced by missing ligands can introduce stepped  $\text{NH}_3$  sorption with a strong hysteresis into the UiO type MOFs (*i.e.*, biphenyl ligands are replaced by pyridine ligands).<sup>112</sup>

## 5. $\text{NO}_x$

Nitrogen oxides ( $\text{NO}_x = \text{N}_2\text{O}$ ,  $\text{NO}$ ,  $\text{N}_2\text{O}_3$ ,  $\text{NO}_2$ ,  $\text{N}_2\text{O}_4$  and  $\text{N}_2\text{O}_5$ ) are considered one of the major air pollutants generated by anthropogenic activities, particularly those that involve fuel combustion from stationary and mobile sources such as thermal power plants and vehicles.<sup>114</sup> It has been estimated that fossil fuel combustion generates around 5% of  $\text{NO}_2$ , and 95%  $\text{NO}$ .<sup>114</sup> Nevertheless, once  $\text{NO}$  is released into the atmosphere, it rapidly reacts with  $\text{O}_2$  to form  $\text{NO}_2$ . The latter is a poisonous red-orange gas responsible for the reddish-brown colour of the smog, although at lower temperatures it can dimerize into a colourless  $\text{N}_2\text{O}_4$  dimer. Due to the highly reactive nature of  $\text{NO}_x$ , the uncontrolled emissions of such gases into the atmosphere are associated with a series of health and environmental issues.<sup>114–116</sup> For instance, the presence of high concentrations of  $\text{NO}_2$  has been directly related to the formation of tropospheric ozone  $\text{O}_3$ ,<sup>109,116</sup> which not only is considered an important greenhouse gas; but is also associated with pulmonary and chronic respiratory diseases.<sup>115,116</sup> The adverse effects caused by atmospheric  $\text{NO}_2$  have motivated an intense research for the development of  $\text{NO}_2$  abatement technologies.<sup>114,117</sup>

One of the most studied methods to mitigate the atmospheric  $\text{NO}_2$  is the development of porous materials for the selective capture of this pollutant. The traditional adsorbent materials used for  $\text{NO}_2$  removal include zeolites,<sup>118</sup> calcium-based adsorbents,<sup>119</sup> and activated carbon.<sup>120</sup> However, such materials are typically affected by the reactive oxidative nature

of  $\text{NO}_2$ , which hampers the fully reversible desorption of the guest molecules and limits the material regeneration.<sup>117</sup>

### 5.1 MOFs for $\text{NO}_x$ capture

Current investigations in  $\text{NO}_x$  sorption have pointed out that MOFs represent an attractive alternative for storage, selective separation, and/or catalytic transformation of  $\text{NO}_2$ .<sup>121</sup> Such materials not only display a large surface area, but they also exhibit tuneable pore functionalities<sup>122</sup> allowing for the stabilisation of guest molecules through the formation of supramolecular host-guest interactions. For instance, a study reported by Peterson *et al.*<sup>123</sup> points out the key role of the organic linker for the capture of  $\text{NO}_2$ . In this work, the authors conducted a comparative study about the  $\text{NO}_2$  sorption performance of UiO-66 and UiO-66- $\text{NH}_2$ .

The gas sorption experiments were performed under dry and controlled humid conditions. The results obtained from the microbreakthrough experiments reveal that UiO-66- $\text{NH}_2$  exhibits a higher capacity for the  $\text{NO}_2$  sorption than UiO-66 ( $20.3 \text{ mmol g}^{-1}$  vs.  $8.8 \text{ mmol g}^{-1}$ ; respectively). Under humid conditions (80% RH), UiO-66- $\text{NH}_2$  exhibits higher uptake of  $\text{NO}_2$  than under dry conditions ( $31.2 \text{ mmol g}^{-1}$  vs.  $20.3 \text{ mmol g}^{-1}$ ; respectively), and it produces a significantly lower amount of  $\text{NO}$  as a by-product than its analogous UiO-66 (4.5%, 9.5%; respectively).

Such differences were explained in terms of the higher capability of UiO-66- $\text{NH}_2$  to adsorb  $\text{H}_2\text{O}$  vapours. As the  $\text{H}_2\text{O}$  co-adsorbed within the pore network might enhance the stabilization of  $\text{NO}_2$  molecules through the formation of supramolecular interactions and it facilitates the preferential formation of nitrous acid as a by-product. The complementary characterization of UiO-66- $\text{NH}_2$  upon  $\text{NO}_2$  adsorption revealed that although the crystallinity of UiO-66- $\text{NH}_2$  remains intact, the high reactivity of the adsorbate leads to a series of reactions with the organic linker, which ends up in the post functionalization of the phenyl group (Fig. 23).<sup>123</sup>

The main transformation that suffered the organic linker upon  $\text{NO}_2$  uptake were the nitration of the aromatic ring and the formation of the diazonium ion at the amino group, while in the



Fig. 23 (a) Structure of UiO-66 analogues. Post functionalization of phenyl ring modifications upon  $\text{NO}_2$  sorption: (b) nitration of the phenyl ring, (c) diazonium ion formation. (d) Nitration of the bridging hydroxyl group at the SBU. Reprinted (adapted) with permission from ref. 123. Copyright (2016) John Wiley & Sons.





Fig. 24 Views of the structural model of  $\text{MFM-300(Al)} \cdot (\text{NO}_2)(\text{N}_2\text{O}_4)_2$ . Al-green, C-grey, O-red, H-white, N-blue. (a) and (b) host-guest supramolecular interactions. (c) Structural view of 1D helical chain  $(\text{NO}_2, \text{N}_2\text{O}_4)_\infty$  within the channel of  $\text{MFM-300(Al)}$ . (d) Comparison of IAST selectivities for equimolar mixtures of  $\text{NO}_2/\text{SO}_2$  and  $\text{NO}_2/\text{CO}_2$  at 0.1–1.0 bar for  $\text{MFM-300(Al)}$  at 298 K. (e) Dimensionless breakthrough curve of 0.5%  $\text{NO}_2$  (5000 ppm) diluted in  $\text{He}/\text{N}_2$  under both dry and wet conditions through a fixed bed packed with  $\text{MFM-300(Al)}$  at 298 K and 1 bar. Reprinted (adapted) with permission from ref. 124. Copyright (2018) Springer Nature.

inorganic SBU the terminal  $-\text{OH}$  group is replaced by the  $\text{NO}^{3-}$  ion. More recently, a study conducted by Schröder and Yang,<sup>124</sup> demonstrated that the synergistic effect between the organic ligand and the inorganic building block in  $\text{MFM-300(Al)}$  allows for the stabilisation of highly reactive  $\text{NO}_2$  species within the pore network (Fig. 24a–c). The authors reported that under ambient conditions  $\text{MFM-300(Al)}$  exhibits a fully reversible  $\text{NO}_2$  isotherm uptake of  $14.1 \text{ mmol g}^{-1}$  at 298 K. Moreover, the host material retains its crystallinity and sorption capacity after five cycles of  $\text{NO}_2$  adsorption/desorption. Remarkably,  $\text{MFM-300(Al)}$  displays outstanding performance for the selective removal of low-concentration of  $\text{NO}_2$  (5000 to  $<1$  ppm) from gas mixtures (Fig. 24d). The optimal uptake and selectivity of  $\text{MFM-300(Al)}$  for  $\text{NO}_2$  was attributed to the existence of both host-guest and guest-guest interactions. The former involves mainly the hydrogen bonding interaction between  $\text{NO}_x$  and the  $-\text{OH}$  pendant group of the inorganic node, while the latter refers to the supramolecular interactions between the guest molecules in their monomeric ( $\text{NO}_2$ ) and dimeric ( $\text{N}_2\text{O}_4$ ) form. Such interactions give rise to a one-dimensional helical chain arrangement comprised of alternating monomer-dimer molecules

$(\text{NO}_2 \cdot \text{N}_2\text{O}_4)_\infty$  running along the channel of  $\text{MFM-300(Al)}$  (Fig. 24d).

The cooperative supramolecular interactions between  $\text{NO}_2$  and  $\text{N}_2\text{O}_4$ , confined within the pore network, allows for the stabilization of the highly reactive  $\text{NO}_2$  molecules and inhibits the guest–host electron transfer. This affords an unusual, fully reversible desorption of  $\text{NO}_2$  without altering the framework structure of the host material. The structural versatility of MOFs not only permits the stabilization of highly reactive  $\text{NO}_x$  species within the pore channels but also opens the possibility for the catalytic conversion of  $\text{NO}_x$  into more valuable and/or less abrasive compounds. In this regard, Schröder and Yang reported the adsorption and catalytic transformation of  $\text{NO}_2$  by using a redox-active MOF,<sup>125</sup> termed  $\text{MFM-300(V)}$  [ $\text{V}_2(\text{OH})_2(\text{C}_{16}\text{H}_6\text{O}_8)$ ]. This system not only exhibits high adsorption capacity for  $\text{NO}_2$  ( $13 \text{ mmol g}^{-1}$  at 298 K and 1.0 bar), but it also allows for the catalytic reduction of  $\text{NO}_2$  into  $\text{NO}$ . The structural analysis reveals that upon gas sorption,  $\text{NO}_2$  molecules get primarily anchored to the pore walls through a hydrogen-bonding interaction with the bridging hydroxyl groups of the inorganic nodes. Further stabilization is reached by forming of 8-fold supramolecular interactions with the aromatic ligand (Fig. 25). Then, those interactions give rise to the host–guest charge transfer process and the formation of  $\text{NO}$  (through the oxidation of the metal centre from  $\text{V}^{3+}$  to  $\text{V}^{4+}$ ), and water, which is produced by the deprotonation of the bridging  $-\text{OH}$  groups anchored to the SBU.

Recent research conducted by Dincă and co-workers highlights the capacity of  $\text{M-MFU-4l}$  ( $\text{M} = \text{Cu}, \text{Zn}$ ) MOFs for  $\text{NO}$  capture and on-demand desorption of guest molecules by a thermal treatment.<sup>126</sup> In this study, the authors demonstrated that the gas-sorption properties of the host material can be easily adjusted by modifying the cation identity and the oxidation state of the inorganic building block. To this aim, three different systems were selected as host materials (i)  $\text{Zn}_5\text{Cl}_4(\text{BTDD})_3$ ; (ii)  $\text{Zn}_3\text{Cu}_2\text{Cl}_4(\text{BTDD})_3$ ; and (iii)



Fig. 25 Rapid scan RS model showing the packing of guest molecules within  $\text{MFM-300(V}^{3+})$ . Reprinted with permission from ref. 125. Copyright (2020) American Chemical Society.



$\text{Zn}_3\text{Cu}_2\text{Cl}_2(\text{BTDD})_3$  ( $\text{H}_2\text{BTDD} = \text{bis}(1\text{H}-1,2,3\text{-triazolate}[4,5\text{-}b;4',5'\text{-}i])\text{dibenzo}[1,4]\text{ dioxin}$ ). The first material  $\text{Zn}_5\text{Cl}_4(\text{BTDD})_3$  ( $\text{Zn-MFU-4l}$ ) displayed the lowest capacity for NO sorption ( $0.51 \text{ mmol g}^{-1}$  at 750 torr). The second system,  $\text{Zn}_3\text{Cu}_2\text{Cl}_4(\text{BTDD})_3$  ( $\text{Cu}^{\text{II}}\text{-MFU-4l}$ ), was obtained by substituting two  $\text{Zn}^{2+}$  atoms from  $\text{Zn-MFU-4l}$  by  $\text{Cu}^{2+}$  ions. This subtle modification resulted in a significant increase in the NO sorption capacity ( $1.43 \text{ mmol g}^{-1}$  at 750 torr).

These findings were explained in terms of the differences in the tetrahedral coordination environment around the metal centre  $\text{N}_3\text{M-Cl}$  ( $\text{M} = \text{Zn}^{2+}, \text{Cu}^{2+}$ ). In the first case, the saturated coordination environment around  $\text{Zn}^{2+}$  prevents the formation of stronger metal-NO interactions, whereas in the second system, the  $\text{N}_3\text{Cu-Cl}$  geometry is sufficiently distorted to allow the NO molecules to approach closer to the metal centre leading to stronger Cu-NO interactions. The formation of  $\text{Cu}^{2+}$ -nitrosyl species upon NO adsorption was corroborated by diffuse-reflectance infrared Fourier-transform spectroscopy (DRIFT) study. Finally, the third system ( $\text{Cu}^+\text{-MFU-4l}$ ) was obtained by the reduction of  $\text{Cu}^{2+}$  to  $\text{Cu}^+$  accompanied by the concomitant loss of chloride. This system displays a significant improvement in the low-pressure NO uptake ( $1.24 \text{ mmol g}^{-1}$  below 1.4 torr). This value is three times the amount of NO adsorbed by  $\text{Cu}^{2+}\text{-MFU-4l}$  ( $0.0008 \text{ mmol g}^{-1}$ ) and  $\text{Zn}^{2+}\text{-MFU-4l}$  ( $0.0002 \text{ mmol g}^{-1}$ ) under the same conditions. The DRIFT analysis suggests that the metal centre in  $\text{Cu}^+\text{-MFU-4l}$  allows for the formation of  $\text{Cu}^+\text{-NO}$  complex even when the material is exposed to low concentrations of NO in Ar (10 ppm). This interaction favours the NO disproportionation  $3 \text{ NO} \rightarrow \text{NO}_2 + \text{N}_2\text{O}$  and the oxidation of the metal centre to  $\text{Cu}^{2+}$  which strongly binds to the  $\text{NO}_2$  product (Fig. 26). Then, the  $\text{Cu}^{2+}$ -nitrite bond can be cleaved by exposing  $\text{Cu}^{2+}\text{-MFU-4l}(\text{NO}_2)$  to high temperatures, releasing

the anchored  $\text{NO}_2$  and thereby regenerating the adsorbent  $\text{Cu}^+\text{-MFU-4l}$ . According to the authors, this catalytic system represents a potentially attractive scheme for cold-start NO capture. The design of porous materials for storage and controlled release of NO have gained relevance in biomedicine, as it has been shown that the exposure to controlled doses of NO induces wound healing and prevents the formation of blood clots. Moreover, NO is a potent antimicrobial agent; therefore, the development of materials for the local release of NO could be highly advantageous to reduce the risk of infections.

One of the first reports about the use of MOFs for the on-demand delivery of NO was published in 2007 by Morris and co-workers.<sup>127</sup> In this work, the authors used HKUST-1 as a reservoir for NO. The gravimetric adsorption experiments performed at 196 K and 298 K display significant isotherm hysteresis with an adsorption capacity of *ca.*  $9 \text{ mmol g}^{-1}$  and  $3 \text{ mmol g}^{-1}$  at one bar, respectively. Upon gas desorption processes, both isotherms exhibit a remaining amount of NO trapped within the pore network ( $2 \text{ mmol g}^{-1}$ ). The IR analysis of NO-loaded material reveals that the presence of open copper sites in the walls of HKUST-1 framework allows for the formation of  $\text{NO}\cdots\text{Cu}^{2+}$  coordination adduct; thereby leading to the irreversible adsorption of NO. However, NO molecules trapped within the pore network can be released on demand upon exposure of the NO-loaded HKUST-1 to water vapours, as  $\text{H}_2\text{O}$  acts as a nucleophile replacing the NO molecules coordinated to the open copper sites.

More recently, the same research group reported the development of MOF-based composites for the controlled delivery of NO.<sup>128</sup> The selected host material was CPO-27-Ni, as this MOF affords highly efficient adsorption, storage, and release cyclable profile for NO.<sup>129</sup> Moreover, this material exhibits high stability towards adsorbed water, which allows for the controlled release of NO when exposed to moisture, without altering the structural arrangement of the host material.

The optimal MOF films were obtained by varying the amount of CPO-27-Ni (wt%) integrated within a polyurethane matrix. The composite films exhibited homogeneous distribution of the MOF within the polymer matrix. The release of NO was triggered by exposing the composite films to 11% or relative humidity. Such conditions allow for the controlled release of the NO adsorbed without affecting the polymer properties. Finally, the antimicrobial properties of the resultant MOF-based composite demonstrated that the controlled release of biologically active levels of NO provides a bactericidal effect against *Escherichia coli* (*E. coli*) and *Staphylococcus aureus* (*S. aureus*).

## 6. Selectivity of trace gases

One important aspect of evaluating MOF materials is their selectivity of adsorbing one gas preferentially over other molecules that are present in the industrial flue gas streams, as these are mainly composed of  $\text{CO}_2$  (10–15% [v]),  $\text{N}_2$  (70–75% [v]), and  $\text{H}_2\text{O}$  ( $\sim 10\text{--}18\%$  [v]),<sup>130</sup> whereas gases such as  $\text{SO}_2$  (0.00325% [v], 500–3000 ppm),  $\text{H}_2\text{S}$  (13.5% [v], 1000–4000 ppm),  $\text{NH}_3$  (300–800 ppm) and  $\text{NO}_x$  (200–800 ppm) are present in trace concentrations.<sup>131</sup> For this reason, it is highly desirable that the study of the capture of trace



Fig. 26 Proposed NO Disproportionation Cycle Using  $\text{Cu}^{\text{I}}\text{-MFU-4l}$ . During the thermal decomposition of  $\text{Cu}^{\text{II}}\text{-MFU-4l}(\text{NO}_2)$ , NO is the major  $\text{NO}_x$  species detected. Reprinted with permission from ref. 126. Copyright (2021) American Chemical Society.





gases by MOFs should be accompanied by a selectivity study in the presence of other gases in order to have a complete profile of their potential applications at industrial levels.

Table 4 lists the most promising MOF materials for the separation of SO<sub>2</sub> and H<sub>2</sub>S gases, with a good selectivity performance.

## 7. Stability and reusability of MOFs

As previously shown, there is a wide variety of MOFs with high structural stability towards corrosive gases (SO<sub>2</sub>, H<sub>2</sub>S, NH<sub>3</sub> and NO<sub>x</sub>). The stability, as well as the reusability of the MOFs, is required for tangible industrial applications on the adsorption field. Considering that the CSD currently contains near to 70 000 MOF structures,<sup>143</sup> a selection criterion for MOFs that could be potentially useful in the adsorption of toxic gases is essential, as are the guidelines for generating new materials focused on this target.<sup>144</sup> Although the nature of MOFs is very

diverse, MOFs stable in the presence of corrosive gases feature some common characteristics: (i) the strength of the ligand-metal bond; (ii) oxidation state of the metal centre; (iii) robustness of the metallic cluster; and (iv) the formation of supramolecular host-guest interactions. The presence of at least one of these characteristics is responsible for the stabilization of the framework under such harsh conditions. For example, when the strongest binding site corresponds to a free metal site, the metal-ligand bond should be strong enough to avoid linker displacement and subsequent structure degradation. The combination of ligands with strong donor groups/atoms and late transition metals, or the use of metals with a higher oxidation state together with carboxylate ligands are good synthetic strategies to improve the strength of the metal-ligand bonds and, therefore, increase the overall stability of the framework.<sup>21,40a,145</sup> For example, MOFs formed by triazolate ligands such as the M<sub>2</sub>Cl<sub>2</sub>BTDD family (M = Ni<sup>2+</sup>, Co<sup>2+</sup>, Mn<sup>2+</sup>, and Cu<sup>2+</sup>)<sup>107</sup> with uncoordinated metal sites are stable even after

**Table 4** Summary of the adsorption captures of SO<sub>2</sub> and H<sub>2</sub>S and IAST selectivity of each one in various MOFs materials

Gas target	MOF	Gas adsorption [mmol g <sup>-1</sup> ]	Flue gas concentration	Selectivity				Ref.
				CO <sub>2</sub>	N <sub>2</sub>	CH <sub>4</sub>	Other gases	
SO <sub>2</sub>	MIL-160	7.2	SO <sub>2</sub> /CO <sub>2</sub> (10 : 90–50 : 50 v/v)	124–128 (IAST)	31.25 <sup>37e</sup>	—	—	18
	MIL-125(Ti)-NH <sub>2</sub>	10.8	SO <sub>2</sub> /CO <sub>2</sub> (10 : 90–50 : 50 v/v)	42–55 (IAST)	—	—	—	18
	MFM-170	17.5	Equimolar SO <sub>2</sub> /N <sub>2</sub>	35	944	260	203 (CO)	19
	MFM-300(Al)	7.1	50–350 mbar <sup>b</sup>	—	6522	3620	10 <sup>5</sup> (H <sub>2</sub> ) 3105(CO) 4974 (O <sub>2</sub> )	37a
	MFM-300(In)	8.28	At 50 : 50 mixture of each gas	60	5000	425	—	37b
	MFM-601	12.3	SO <sub>2</sub> /CO <sub>2</sub> , SO <sub>2</sub> /N <sub>2</sub> (50 : 50 to 10 : 90)	32	255	—	—	132
	ELM-12	2.73	10 : 90 mixture at 298 K and 1 bar	30	4064	871	—	133
	1@Ba(OH)2	4.0 <sup>a</sup>	N <sub>2</sub> /CO <sub>2</sub> /SO <sub>2</sub> (83.5 : 14 : 2.5 v/v)	990	—	—	—	45
	SIFSIX-1-Cu	11.01	At 10 : 90 mixture of each gas	70.7	3145.7	1241.4	—	51
	SIFSIX-2-Cu-i	6.9	At 10 : 90 mixture of each gas	87.1	3103.2	1017.1	—	51
	SIFSIX-3-Zn	2.1	At 10 : 90 mixture of each gas	—	506.7	276	—	51
	SIFSIX-3-Ni	2.74	At 10 : 90 mixture of each gas	—	701.8	371.6	—	51
	KAUST-7	1.4 <sup>a</sup>	SO <sub>2</sub> /CO <sub>2</sub> /N <sub>2</sub> (4%:4% : balance) and (500 ppm : 10% : balance)	1	—	—	—	52
	KAUST-8	1.6 <sup>a</sup>	SO <sub>2</sub> /CO <sub>2</sub> /N <sub>2</sub> : 0.05/10/89.95	66	—	—	—	52
	ECUT-77	8.0	SO <sub>2</sub> /CO <sub>2</sub> (1 : 99 v/v; 2000 ppm SO <sub>2</sub> )	44–36	—	—	—	134
	ECUT-100	4.95	At 1 : 99 mixture of each gas	27.5–26.9	—	2302	—	135
	ECUT-111	11.56	SO <sub>2</sub> /CO <sub>2</sub> , SO <sub>2</sub> /N <sub>2</sub> (1 : 99 v/v)	22.2–25.2	860.9	—	—	136
H <sub>2</sub> S	MIL-101(Cr)	0.419 <sup>a</sup>	H <sub>2</sub> S/CO <sub>2</sub> /He (1 : 10 : 89 v/v)	5	—	—	—	63
	HKUST-1	~1 <sup>a</sup>	H <sub>2</sub> S/CO <sub>2</sub> /He (1 : 10 : 89 v/v)	~40	—	—	—	63
	KAUST-7	—	H <sub>2</sub> S/CO <sub>2</sub> /CH <sub>4</sub> (20 : 20 : 60)	—	—	20.7 <sup>d</sup>	—	139
	KAUST-8	—	H <sub>2</sub> S/CO <sub>2</sub> /CH <sub>4</sub> (20 : 20 : 60)	—	—	18.6 <sup>d</sup>	—	139
	KAUST-8	—	H <sub>2</sub> S/CO <sub>2</sub> /CH <sub>4</sub> (5 : 5 : 90)	1	—	—	—	137
	SIFSIX-2-Ni-i	—	H <sub>2</sub> S/CO <sub>2</sub> /CH <sub>4</sub> (5 : 5 : 90)	3.3	—	—	—	137
	MIL-125(Ti)-NH <sub>2</sub>	—	H <sub>2</sub> S 0.001	—	—	70 <sup>e</sup>	—	138
	Ga-soc-MOF-1a	4.4	CO <sub>2</sub> /H <sub>2</sub> S/CH <sub>4</sub> (5% : 5% : 90%)	7	—	—	—	64
	Y-fum-fcu-MOF	1.1 <sup>a</sup>	CO <sub>2</sub> /H <sub>2</sub> S/CH <sub>4</sub> (5% : 5% : 90%)	6.4	—	—	—	139
	[BMIM][Cl]/Cu-TDPAT <sup>e</sup>	—	H <sub>2</sub> S 1000 ppm	—	—	1302	—	140
	Cu-TDPAT <sup>e</sup>	—	H <sub>2</sub> S 1000 ppm	—	—	141	—	140
	MIL-53(Al) <sup>f</sup>	—	CH <sub>4</sub> /CO <sub>2</sub> /H <sub>2</sub> S (60% : 39.9% : 0.1%)	—	—	23–34	—	141
	MIL-47(V)-Br <sup>g</sup>	—	H <sub>2</sub> S/CH <sub>4</sub> (5 : 95) 0.1 MPa	—	278	68	—	142
	MIL-47(V) <sup>g</sup>	—	H <sub>2</sub> S/CH <sub>4</sub> (5 : 95) 0.1 MPa	—	179	223	—	142
			H <sub>2</sub> S/CH <sub>4</sub> (1 : 99) 0.1 MPa			51		
			H <sub>2</sub> S/N <sub>2</sub> (50 : 50)					

<sup>a</sup> Breakthrough experimental result. <sup>b</sup> Obtained from ratio of slopes of initial adsorption isotherm plot at a low pressure region. <sup>c</sup> GCMC simulations at 303 K and 10 bar. <sup>d</sup> Membrane composite measured at 35 °C. <sup>e</sup> Composite materials. <sup>f</sup> Pellets. <sup>g</sup> GCMC simulations at 273 K.



several sorption and desorption cycles of  $\text{NH}_3$ . Such stability increases according to the Irving–Williams series, being the  $\text{Ni}^{2+}$  framework more stable than the  $\text{Cu}^{2+}$ . In this case, the presence of heterolytic metal–ligand bonds and a less labile metal centre, enhances the MOF's stability. In MFM-170,<sup>19</sup> a MOF formed by the  $\text{Cu}^{2+}$  paddlewheel SBU, the coordination of one of the  $\text{Cu}^{2+}$  centres to a N-donating ligand, allowed reversible  $\text{SO}_2$  adsorption, even if one of the  $\text{Cu}^{2+}$  atoms presented weak contacts with  $\text{SO}_2$ . Additionally, the interactions between  $\text{SO}_2$  and the surface of the framework contributed to the reversibility of the adsorption process. This research represents an example of enhancing the chemical stability of a MOF by increasing the metal–ligand bond strength, a highly effective strategy to increase the stability of MOFs with labile metals.

On the other hand, the use of small metal cations confers stability against chemical degradation, as shown for several MOFs constructed with trivalent and tetravalent cations such as  $\text{Al}^{3+}$ ,  $\text{In}^{3+}$ ,  $\text{Sc}^{3+}$ , and  $\text{Cr}^{3+}$  and  $\text{Zr}^{4+}$ ,  $\text{V}^{4+}$ , and  $\text{Ti}^{4+}$ , respectively. These metal centres tend to form robust clusters, increasing the stability of the framework towards corrosive gases. For example, MIL-101(Cr) and MIL-101(Cr)-4F(1%) formed by  $[\text{Cr}_3(\mu_3\text{-O})(\text{O}_2\text{CR})_6]$  clusters, are stable to  $\text{SO}_2$  and  $\text{H}_2\text{S}$ ;<sup>20,34</sup> Mg-CUK-1 with  $[\text{Mg}_3(\mu_3\text{-OH})]^{5+}$  clusters is stable to  $\text{H}_2\text{S}$ ;<sup>68</sup> MIL-53(Al)-TDC formed by *trans*-corner-sharing  $[\text{Al}(\mu_2\text{-OH})(p\text{-BDC})]$  polyhedra is stable to  $\text{H}_2\text{S}$ .<sup>69</sup> Additionally, the MFM-300 family formed by infinite chains of  $[\text{M}_2(\mu_2\text{-OH})_2(\text{C}_{16}\text{O}_8\text{H}_6)]$  ( $\text{M} = \text{Al}^{3+}$ ,  $\text{In}^{3+}$ ,  $\text{Sc}^{3+}$ ,  $\text{V}^{3+}$ ), has demonstrated to be stable to  $\text{SO}_2$ ,  $\text{H}_2\text{S}$ ,  $\text{NH}_3$ , and  $\text{NO}_2$ .<sup>37,70,110,111,125</sup> This family represents an excellent example of how the non-covalent interactions formed between the framework surface and the host molecules provide to the additional structural stability and adsorption reversibility in almost all the studied cases. The principal interaction involves the  $\mu_2\text{-OH}$  motif as hydrogen bond donor and the gas molecule as an acceptor, followed by guest–ligand and guest–guest interactions. This last aspect has a direct impact on the recyclability of the MOF, where most of the materials with good cyclability exhibit similar host–guest interactions such as hydrogen bonds (strong and weak), electrostatic interactions inside the pore framework, and metal–guest interactions. For example: MFM-170,<sup>19</sup> MIL-101(Cr)-4F(1%),<sup>20</sup> are stable even after 50  $\text{SO}_2$  adsorption–desorption cycles while the following MOFs are stable for different numbers of  $\text{SO}_2$  cycles  $[\text{Ni}_8(\text{OH})_4(\text{H}_2\text{O})_2(\text{-BDP-X})_6]$  (10 cycles),<sup>45</sup> SIFSIX-1-Cu (4–6 cycles),<sup>51</sup> and MFM-300(Sc) (10 cycles).<sup>37c</sup> Furthermore, Mg-CUK-1,<sup>68</sup> MIL-53(Al)-TDC,<sup>69</sup> and MFM-300(Sc)<sup>70</sup> are stable for at least five adsorption–desorption cycles of  $\text{H}_2\text{S}$  while  $\text{Mg}_2(\text{dobpdc})$ ,<sup>109</sup>  $\text{Co}_2\text{Cl}_2$  BBTA and  $\text{Co}_2\text{Cl}_2$  BTDD,<sup>108</sup> MFM-300(Al) (50 cycles),<sup>111</sup> and UiO-67.<sup>112</sup> Finally, MFM-300(Al) is not affected even by five cycles of  $\text{NO}_2$ .<sup>124</sup>

## 8. Conclusions and future perspectives

Air pollution due to the emissions of toxic gases is the single largest environmental health risk around the world since it is responsible for one in eight premature global deaths, reduction

of the biodiversity, crop damages and acidification of soils and waters. Thus, the development of efficient technologies for the capture of toxic gases (*i.e.*,  $\text{NO}_x$ ,  $\text{SO}_2$ ,  $\text{NH}_3$  and  $\text{H}_2\text{S}$ ) from static and mobile sources is essential, in order to achieve a cleaner environment. MOFs are amongst the most promising candidates for the capture of these toxic gases since their sorption selectivity is directly tuneable as a function of the topology and chemical composition of the pores, which can optimise the interactions between MOFs and these toxic molecules, affording enhanced gas adsorption properties. Although the main drawback of MOFs is their vulnerability to these highly corrosive gases which can compromise their chemical stability, remarkable examples have demonstrated high chemical stability to  $\text{NO}_x$ ,  $\text{SO}_2$ ,  $\text{NH}_3$  and  $\text{H}_2\text{S}$ .

Chemically stable MOFs for the capture of  $\text{SO}_2$  have provided promising advances in the field and the understanding of the role of different chemical functionalities, is the key for accomplishing superior  $\text{SO}_2$  captures. Coordinatively unsaturated metal sites (open metal sites) incorporated into chemical stable MOFs (*e.g.*, MFM-170 and MIL-101(Cr)-4F(1%)) demonstrated the relevance of the interaction of these open metal sites and  $\text{SO}_2$  molecules. The design of new functionalised MOF materials with coordinatively unsaturated metal sites signifies an interesting alternative to obtain superior  $\text{SO}_2$  captures and therefore, the challenge is to be able to also incorporate chemical stability to these MOFs. Thus, high  $\text{SO}_2$  uptakes are related to large BET surface area, pore size and the open metal sites incorporation into MOFs, while structural (chemical) stability is associated with the type of metal, and the interactions adsorbate–adsorbent inside the pore.

Hydroxo-functionalisation ( $\mu\text{-OH}$  groups) in structural stable MOFs (*e.g.*, MFM-300(M)) have shown excellent capabilities for the capture and detection of  $\text{SO}_2$  with high chemical stability and excellent cyclability involving a remarkably facile regeneration. The key for all of such outstanding properties is the preferential interaction between the functional group ( $\mu\text{-OH}$ ) and  $\text{SO}_2$ , in which the  $\mu\text{-OH}$  groups binds  $\text{SO}_2$  molecules through the formation of  $\text{O}=\text{S}=\text{O}(\delta^-)\cdots\text{H}(\delta^+)\text{-O}$  hydrogen bonds, reinforced by weak supramolecular interactions with C–H atoms from the aromatic rings of the framework. The chemical stability of the MFM-300(M) family relies on the strength of the coordination bonds between the oxygen atoms form the carboxylic ligand (biphenyl-3,3',5,5'-tetracarboxylic acid) and the  $\text{M}^{3+}$  metal centres.

Defective sites *a.k.a.*, crystal irregularities, composition inhomogeneities or defects in MOFs have exhibited increased  $\text{SO}_2$  adsorption capacities, energies, and  $\text{SO}_2/\text{CO}_2$  selectivity. For example, in nickel pyrazolate MOFs it was demonstrated that the pre-synthetic introduction of amino and hydroxyl functional groups on the organic linkers and the post-synthetic modifications, synergistically increase the  $\text{SO}_2$  capture capacity of these MOF materials.

Halogen functionalised MOF materials (*e.g.*, hexafluorosilicate ( $\text{SiF}_6^{2-}$ ) incorporation in SIFSIX MOFs) showed highly efficient removal of  $\text{SO}_2$  from other gases, at a very low  $\text{SO}_2$  concentrations, and excellent  $\text{SO}_2/\text{CO}_2$  and  $\text{SO}_2/\text{N}_2$  selectivities. These properties were attributed to the strong



electrostatic interactions between the  $\text{SO}_2$  molecules and the  $\text{SiF}_6^{2-}$  anions ( $\text{S}^{\delta+} \cdots \text{F}^{\delta-}$ ), assisted by dipole–dipole interactions with the ligand ( $\text{O}^{\delta-} \cdots \text{H}^{\delta+}$ ).

The identification of MOFs capable of capturing  $\text{H}_2\text{S}$  under industrially practical pressure-swing desorption conditions, symbolises a very promising application which is based on the chemical stability of these materials. For example, stable MOF materials constructed with  $\mu\text{-OH}$  functional groups (e.g., MIL-53(Al)-TDC) exhibited high and fully reversible  $\text{H}_2\text{S}$  capture where the formation of hydrogen bonds between  $\text{H}_2\text{S}$  and the  $\mu\text{-OH}$  functional group (a relatively weak interaction) facilitates the  $\text{H}_2\text{S}$  cyclability.

The chemical transformation of  $\text{H}_2\text{S}$  within the pores of MOFs to produce, *in situ*, polysulphides is a new and exciting discovery in MFM-300(M) and SU-101 MOF materials. In addition to the promising application as novel MOF-lithium/sulphur batteries, the chemical investigation behind them, provided additional information on the electrochemical potential of MOFs which could guide new interesting properties to be discovered. Then, although the polysulphide formation was explained in terms of a “disproportionation” type reaction (protons of  $\text{H}_2\text{S}$  play the role of an oxidant and the sulphide plays the role of a reducing agent), other hypotheses need to be explored. What if the polysulphide formation is a consequence of reversible metal–ligand bonding upon the adsorption of  $\text{H}_2\text{S}$ ? We anticipate new perspectives will be shortly investigated.

Paradoxically, the role of  $\text{H}_2\text{S}$  as an endogenous biological mediator in the human body is crucial. For example,  $\text{H}_2\text{S}$  executes a vital activity in the regulation of blood pressure, neurotransmission, anti-inflammatory mechanism, anti-oxidation, angiogenesis and apoptosis. Thus, the delivery and detection of  $\text{H}_2\text{S}$  levels in living cells and organisms is an outstanding application for MOF materials. For example, Ni-CPO-27 showed a promising release of  $\text{H}_2\text{S}$  (under physiological conditions) with a short induction period of approximately 5 min. In the field of  $\text{H}_2\text{S}$  detection, for example, a post-synthetic modification of ZIF-90 with malononitrile ( $\text{N}\equiv\text{C}-\text{CH}_2-\text{C}\equiv\text{N}$ ), exhibited a specific reaction with  $\text{H}_2\text{S}$  completing an enhancement of photoluminescence, which constitutes the base for the detection of  $\text{H}_2\text{S}$ . Thus, the development of this research is expanding by the fundamental principle of introducing a reactive site for  $\text{H}_2\text{S}$  within MOF material (monitored by fluorescence), which can work under physiological pH, to detect exogenous  $\text{H}_2\text{S}$  in living cells, while the MOF-probe shows low toxicity and high biocompatibility.

Although most MOF materials have exhibited poor chemical stability towards  $\text{NH}_3$ , chemically stable MOFs constructed with different chemical functionalities have shown interesting  $\text{NH}_3$  capture performances.

Coordinationally unsaturated metal sites incorporated, for example, in bisbenzenetriazolate and triazolate MOFs, showed high and reversible  $\text{NH}_3$  uptakes with strong interactions between the open metal sites and  $\text{NH}_3$ . The chemical stability of these MOF materials was attributed to the strength of the N atom coordinated to divalent metal centres.  $\text{Mg}_2(\text{dobpdc})$  demonstrated high  $\text{NH}_3$  capture and chemical stability to not only dry  $\text{NH}_3$ , but also to wet  $\text{NH}_3$ . Interestingly, it was

experimentally and computationally demonstrated that  $\text{NH}_3$  was preferentially adsorbed, by coordination bonds, to the coordinatively unsaturated metal sites of  $\text{Mg}_2(\text{dobpdc})$ . The exceptional chemical stability of this  $\text{Mg}^{2+}$ -based MOF material credited to the higher affinity of  $\text{Mg}^{2+}$  to oxygen atoms than nitrogen atoms, as confirmed by van der Waals (vdW)-corrected density functional theory (DFT) calculations.

The  $\mu\text{-OH}$  functionalised MFM-300(M) family demonstrated remarkable  $\text{NH}_3$  adsorption properties, high chemical stability, high uptakes and attractive cyclabilities. Not surprisingly, as in the case of  $\text{SO}_2$  and  $\text{H}_2\text{S}$ , the preferential adsorption sites of the MFM-300(M) materials were found at the hydroxo functional group. For example, in the case of MFM-300(Al) the adsorption of  $\text{NH}_3$  showed an atypical adsorption mechanism where adsorbent and adsorbate experienced a rapid site-exchange *via* reversible formation and cleavage of O–H and O–H<sub>(from  $\text{NH}_3$ )</sub> chemical bonds, in other words a pseudo-chemisorption binding mechanism.

As previously described in the  $\text{SO}_2$  capture section, crystal irregularities can provide very particular physical and chemical properties. Then, defects in MOF materials also demonstrated remarkable  $\text{NH}_3$  adsorption properties. For example, UiO-67 and UiO-bpydc containing 4,4'-biphenyl dicarboxylate and 4,4'-(2,2'-bipyridine) dicarboxylate ligands, despite their structural similarities demonstrated a drastic difference in the  $\text{NH}_3$  adsorption properties when the biphenyl groups in the organic ligand were replaced by the bipyridine moieties. Such replacement can confer flexibility to the framework in the context of mainly ligand “flipping” but without significant pore volume alteration.

Current investigations in  $\text{NO}_x$  capture have pointed out that chemical stable MOFs represent an attractive alternative for storage, selective separation, and/or catalytic transformation of  $\text{NO}_2$ . For example, the synergistic effect between the organic ligand and the inorganic building block in MFM-300(Al) showed the stabilisation of highly reactive  $\text{NO}_2$  species within the micropores. The optimal uptake and selectivity of MFM-300(Al) for  $\text{NO}_2$  was attributed to the existence of both host–guest and guest–guest interactions. The former involves mainly the hydrogen bonding interaction between  $\text{NO}_x$  and the hydroxo functional group, while the latter refers to the supramolecular interactions between the guest molecules in their monomeric ( $\text{NO}_2$ ) and dimeric ( $\text{N}_2\text{O}_4$ ) form.

Interestingly, the design of MOF materials for storage and controlled release of NO have gained relevance in biomedicine, as it has been shown that the exposure to controlled doses of NO induces wound healing and prevents the formation of blood clots. For example, CPO-27-Ni exhibited highly efficient adsorption, storage, and release cyclable profile for NO with a high stability to water, allowing a controlled release of NO when exposed to moisture.

Despite the significant progress in the capture of  $\text{NO}_x$ ,  $\text{SO}_2$ ,  $\text{NH}_3$  and  $\text{H}_2\text{S}$  pollutants by MOF-based technology, further research in this field is required to overcome some of the main challenges: chemical stability, reusability, and suitable functionalisation. Considering the large number of MOF materials synthesised to date (over 70 000 structures reported in the





CCD), it is crucial to understand what makes the above-reported MOFs so chemically stable. Thus, this perspective summarises their most important characteristics (metal centre, strength of the metal–ligand bond and functional groups) that should be further investigated in order to be able to design tailor-made MOFs for the capture of corrosive gases. Additionally, an important aspect to consider is the study of breakthrough experiments and selectivity calculations, where more realistic conditions for industrial applications are investigated, providing a direct performance comparison of MOFs to classic materials such as activated carbon, zeolites and metal oxides. On the other hand, the synthesis scalability of MOFs is one of the weak points to contemplate for corrosive gas adsorption applications, as only a few materials can be synthesised on an industrial scale. We desire that this perspective can provide useful information on the significant progress of this field and inspire new investigations to be carried out.

## Author contributions

E. M.-A., M. L. D.-R., and M. J. V.-H. conducted the literature research and drafted the manuscript. V. J. and I. A. I. conceived the topic and structure of the article. Outlined, drafted and supervised the completion of the manuscript. All authors reviewed and contributed to this manuscript.

## Conflicts of interest

There are no conflicts to declare.

## Acknowledgements

The authors thank PAPIIT-UNAM (Grant IN202820), Mexico for financial support. E. M.-A. thanks to CONACYT for the PhD fellowship (770954). M. L. D.-R. thanks Mississippi State University for the financial support. Thanks to U. Winnberg (Pharma View Consulting SC) for scientific discussions and G. Ibarra-Winnberg for conceptualising the design of this contribution.

## Notes and references

- 1 R. A. Silva, J. J. West, J.-F. Lamarque, D. T. Shindell, W. J. Collins, G. Faluvegi, G. A. Folberth, L. W. Horowitz, T. Nagashima, V. Naik, S. T. Rumbold, K. Sudo, T. Takemura, D. Bergmann, P. Cameron-Smith, R. M. Doherty, B. Josse, I. A. MacKenzie, D. S. Stevenson and G. Zeng, *Nat. Clim. Change*, 2017, 7, 647–651.
- 2 World Health Organization, [https://www.who.int/en/news-room/fact-sheets/detail/ambient-\(outdoor\)-air-quality-and-health](https://www.who.int/en/news-room/fact-sheets/detail/ambient-(outdoor)-air-quality-and-health), accessed December 2020.
- 3 K. Balakrishnan, M. Brauer, N. Bruce, F. Forastiere, N. C. Gouveia, R. M. Harrison, F. J. Kelly, P. L. Kinney, M. Lippmann, S. Mehta, B. Ostro, A. Peters, P. H. N. Saldiva, J. M. Samet, M. J. Utell, M. Zuk, *World Health Organization, Air quality guidelines. Global update 2005. Particulate matter, ozone, nitrogen dioxide and sulfur dioxide*, WHO Regional Office for Europe, Copenhagen, 2006.
- 4 G. Shaddick, M. L. Thomas, P. Mudu, G. Ruggeri and S. Gummy, *npj Clim. Atmos. Sci.*, 2020, 3, 1–5.
- 5 J. Lelieveld, J. S. Evans, M. Fnais, D. Giannadaki and A. Pozzer, *Nature*, 2015, 525, 367–371.
- 6 B. Chu, X. Zhang, Y. Liu, H. He, Y. Sun, J. Jiang, J. Li and J. Hao, *Atmos. Chem. Phys.*, 2016, 16, 14219–14230.
- 7 (a) Y. Wang, P. K. Hopke, D. C. Chalupa and M. J. Utell, *Aerosol Sci. Technol.*, 2015, 45, 1245–1249; (b) R. Figueiredo, P. Nunes, M. Meireles, M. Madaleno and M. C. Brito, *J. Cleaner Prod.*, 2019, 222, 129–142; (c) X. Kan, F. Hedenus and L. Reichenberg, *Energy*, 2020, 195, 117434.
- 8 (a) M. Sharifzadeh, G. Triulzi and C. L. Magee, *Energy Environ. Sci.*, 2019, 12, 2789–2805; (b) J. Guo, W. Jiao, G. Qi, Z. Yuan and Y. Liu, *Chin. J. Chem. Eng.*, 2019, 27, 1361–1373.
- 9 (a) E. Martínez-Ahumada, A. López-Olvera, V. Jancik, J. E. Sánchez-Bautista, E. González-Zamora, V. Martis, D. R. Williams and I. A. Ibarra, *Organometallics*, 2020, 39, 883–915; (b) T. Islamoglu, Z. Chen, M. C. Wasson, C. T. Buru, K. O. Kirlikovali, U. Afrin, M. R. Mian and O. K. Farha, *Chem. Rev.*, 2020, 120(16), 8130–8160.
- 10 (a) K. Dedeker, E. Dumas, B. Lavédrine, N. Steunou and C. Serre, in *Metal-Organic Frameworks (MOFs) for Environmental Applications*, ed. S. K. Ghosh, Elsevier, Amsterdam, 2019, ch. 5, pp. 141–178; (b) A. J. Rieth, A. M. Wright and M. Dincă, *Nat. Rev. Mater.*, 2019, 4, 708–725.
- 11 F. C. Men and H. M. Seip, *Environ. Sci. Policy*, 2004, 7, 253–265.
- 12 (a) M. R. Taylor, E. S. Rubin and D. A. Hounshell, *Technol. Forecast. Soc. Change*, 2005, 72, 697–718; (b) S. Reis, P. Grennfelt, Z. Klimont, M. Amann, H. ApSimon, J.-P. Hettelingh, M. Holland, A.-C. LeGall, R. Mass, M. Posch, T. Spranger, M. A. Sutton and M. Williams, *Science*, 2012, 338, 1153–1154.
- 13 T. Larssen, E. Lydersen, D. Tang, Y. He, J. Gao, H. Liu, L. Dual, H. M. Seip, R. D. Vogt, J. Mulder, M. Shao, Y. Wang, H. Shang, X. Zhang, S. Solberg, W. Aas, T. Okland, O. Eilertsen, V. Angell, Q. Li, D. Zhao, R. Xiang, J. Xiao and J. Luo, *Environ. Sci. Technol.*, 2006, 40, 418–425.
- 14 R. K. Srivastava, W. Jozewicz and C. Singer, *Environ. Prog.*, 2001, 20, 219–228.
- 15 (a) F. Rezaei, A. A. Rownaghi, S. Monjezi, R. P. Lively and C. W. Jones, *Energy Fuels*, 2015, 29(9), 5467–5486; (b) Y. Sun, E. Zwolińska and A. G. Chmielewski, *Crit. Rev. Environ. Sci. Technol.*, 2016, 46, 119–142.
- 16 X. Han, S. Yang and M. Schröder, *Nat. Rev. Chem.*, 2019, 3, 108–118.
- 17 (a) W. P. Mounfield III, C. Han, S. H. Pang, U. Tumuluri, Y. Jiao, S. Bhattacharyya, M. R. Dutzer, S. Nair, Z. Wu, R. P. Lively, D. S. Sholl and K. S. Walton, *J. Phys. Chem. C*, 2016, 120(48), 27230–27240; (b) S. Bhattacharyya, S. H. Pang, M. R. Dutzer, R. P. Lively, K. S. Walton, D. S. Sholl and S. Nair, *J. Phys. Chem. C*, 2016, 120(48),



- 27221–27229; (c) S. Glomb, D. Woschko, G. Makhloufi and C. Janiak, *ACS Appl. Mater. Interfaces*, 2017, **9**, 37419–37434.
- 18 P. Brandt, A. Nuhnen, M. Lange, J. Möllmer, O. Weingart and C. Janiak, *ACS Appl. Mater. Interfaces*, 2019, **11**, 17350–17358.
- 19 G. L. Smith, J. E. Eyley, X. Han, X. Zhang, J. Li, N. M. Jacques, H. G. W. Godfrey, S. P. Argent, L. J. M. McPherson, S. J. Teat, Y. Cheng, M. D. Frogley, G. Cinque, S. J. Day, C. C. Tang, T. L. Easun, S. Rudić, A. J. Ramirez-Cuesta, S. Yang and M. Schröder, *Nat. Mater.*, 2019, **18**, 1358–1365.
- 20 E. Martínez-Ahumada, M. L. Díaz-Ramírez, H. A. Lara-García, D. R. Williams, V. Martis, V. Jancik, E. Lima and I. A. Ibarra, *J. Mater. Chem. A*, 2020, **8**, 11515–11520.
- 21 A. J. Rieth, A. M. Wright and M. Dincă, *Nat. Rev. Mater.*, 2019, **4**, 708–725.
- 22 S. Luo, J. Liu and Z. Wu, *J. Phys. Chem. C*, 2019, **123**, 11772–11780.
- 23 S. Chaturvedi, J. A. Rodríguez, T. Jirsak and J. Hrbek, *J. Phys. Chem. B*, 1998, **102**(36), 7033–7043.
- 24 (a) D. Britt, D. Tranchemontagne and O. M. Yaghi, *Proc. Natl. Acad. Sci. U. S. A.*, 2008, **105**, 11623–11627; (b) T. G. Glover, G. W. Peterson, B. J. Schindler, D. Britt and O. Yaghi, *Chem. Eng. Sci.*, 2011, **66**, 163–170; (c) K. Tan, S. Zuluaga, H. Wang, P. Canepa, K. Soliman, J. Cure, J. Li, T. Thonhauser and Y. J. Chabal, *Chem. Mater.*, 2017, **29**, 4227–4235.
- 25 A. C. Elder, S. Bhattacharyya, S. Nair and T. M. Orlando, *J. Phys. Chem. C*, 2018, **122**, 10413–10422.
- 26 K. Tan, P. Canepa, Q. Gong, J. Liu, D. H. Johnson, A. Dyevoich, P. K. Thallapally, T. Thonhauser, J. Li and Y. J. Chabal, *Chem. Mater.*, 2013, **25**, 4653–4662.
- 27 J. Hungerford, S. Bhattacharyya, U. Tumuluri, S. Nair, Z. Wu and K. S. Walton, *J. Phys. Chem. C*, 2018, **122**, 23493–23500.
- 28 M. Eigen, *Pure Appl. Chem.*, 1963, **6**, 97–115.
- 29 C. Petit, B. Levasseur, B. Mendoza and T. J. Bandoz, *Microporous Mesoporous Mater.*, 2012, **154**, 107–112.
- 30 C. Petit, B. Mendoza and T. J. Bandoz, *ChemPhysChem*, 2010, **11**(17), 3678–3684.
- 31 H. Irving and J. P. Williams, *J. Chem. Soc.*, 1953, 3192–3210.
- 32 L. Feng, K.-Y. Wang, G. S. Day, M. R. Ryder and H.-C. Zhou, *Chem. Rev.*, 2020, **120**(23), 13087–13133.
- 33 L. Hamon, C. Serre, T. Devic, T. Loiseau, F. Millange, G. Férey and G. De Weireld, *J. Am. Chem. Soc.*, 2009, **131**, 8775–8777.
- 34 M. L. Díaz-Ramírez, E. Sanchez-González, J. R. Álvarez, G. A. González-Martínez, S. Horike, K. Kadota, K. Sumida, E. González-Zamora, M. A. Springuel-Huet, A. Gutiérrez-Alejandre, V. Jancik, S. Furukawa, S. Kitagawa, I. A. Ibarra and E. Lima, *J. Mater. Chem. A*, 2019, **7**, 15101–15112.
- 35 R. G. Pearson, *J. Am. Chem. Soc.*, 1963, **85**(22), 3533–3539.
- 36 M. Bosch, M. Zhang and H.-C. Zhou, *Adv. Chem.*, 2014, **2014**, 1155.
- 37 (a) S. Yang, J. Sun, A. J. Ramirez-Cuesta, S. K. Callear, W. I. F. David, D. P. Anderson, R. Newby, A. J. Blake, J. E. Parker, C. C. Tang and M. Schröder, *Nat. Chem.*, 2012, **4**, 887–894; (b) M. Savage, Y. Cheng, T. L. Easun, J. E. Eyley, S. P. Argent, M. R. Warren, W. Lewis, C. Murray, C. C. Tang, M. D. Frogley, G. Cinque, J. Sun, S. Rudić, R. T. Murden, M. J. Benham, A. N. Fitch, A. J. Blake, A. J. Ramirez-Cuesta, S. Yang and M. Schröder, *Adv. Mater.*, 2016, **28**, 8705–8711; (c) J. A. Zárate, E. Sánchez-González, D. R. Williams, E. González-Zamora, V. Martis, A. Martínez, J. Balmaseda, G. Maurin and I. A. Ibarra, *J. Mater. Chem. A*, 2019, **7**, 15580–15584; (d) C. P. Krap, R. Newby, A. Dhakshinamoorthy, H. García, I. Cebula, T. E. Easun, M. Savage, J. E. Eyley, S. Gao, A. J. Blake, W. Lewis, P. H. Beton, M. R. Warren, D. R. Allan, M. D. Frogley, C. C. Tang, G. Cinque, S. Yang and M. Schröder, *Inorg. Chem.*, 2016, **55**, 1076; (e) J.-X. Liu, J. Li, W.-Q. Tao and Z. Li, *Fluid Phase Equilib.*, 2021, **536**, 112963.
- 38 I. A. Ibarra, S. Yang, X. Lin, A. J. Blake, P. J. Rizkallah, H. Nowell, D. R. Allan, N. R. Champness, P. Hubberstey and M. Schröder, *Chem. Commun.*, 2011, **47**, 8304–8306.
- 39 V. Chernikova, O. Yassine, O. Shekhah, M. Eddaoudi and K. N. Salama, *J. Mater. Chem. A*, 2018, **6**, 5550–5554.
- 40 (a) R. D. Shannon, *Acta Crystallogr. A*, 1976, **32**, 751–767; (b) L.-H. Schilling, H. Reinsch and N. Stock, in *The Chemistry of Metal-Organic Frameworks. Synthesis, Characterization, and Applications*, ed. S. Kaskel, WILEY-VCH Verlag GmbH & Co. KGaA, Germany, 2016, vol. 1, ch. 5, pp. 106–108; (c) M. G. Goesten, C. F. Guerra, F. Kapteijn, J. Gascon and F. M. Bickelhaupt, *Angew. Chem., Int. Ed.*, 2015, **54**, 12034–12038.
- 41 S. Kancharlapalli, S. Natarajan and T. K. Ghanty, *J. Phys. Chem. C*, 2019, **123**(45), 27531–27541.
- 42 (a) S. Dissegna, K. Epp, W. R. Heinz, G. Kieslich and R. A. Fischer, *Adv. Mater.*, 2018, **30**, 1704501–1717045; (b) W. Xiang, Y. Zhang, Y. Chen, C.-J. Liu and X. Tu, *J. Mater. Chem. A*, 2020, **8**, 21526–21546.
- 43 (a) O. Kozachuk, I. Luz, F. X. Llabrés i Xamena, H. Noei, M. Kauer, H. B. Albadia, E. D. Bloch, B. Marley, Y. Wang, M. Muhler and R. A. Fischer, *Angew. Chem., Int. Ed.*, 2014, **53**, 7058–7062; (b) J. Canivet, M. Vandichel and D. Farrusseng, *Dalton Trans.*, 2015, 4090–4099; (c) J. Wang, L. Liu, C. Chen, X. Dong, Q. Wang, L. Alfífil, M. R. AlAlouni, K. Yao, J. Huang, D. Zhang and Y. Han, *J. Mater. Chem. A*, 2020, **8**, 4464–4472; (d) R. S. Forgan, *Chem. Sci.*, 2020, **11**, 4546–4562.
- 44 E. López-Maya, C. Montoro, L. M. Rodríguez-Albelo, S. D. A. Cervantes, A. A. Lozano-Pérez, J. L. Cenís, E. Barea and J. A. R. Navarro, *Angew. Chem., Int. Ed.*, 2015, **54**, 6790–6794.
- 45 L. M. Rodríguez-Albelo, E. López-Maya, S. Hamad, A. R. Ruiz-Salvador, S. Calero and J. A. R. Navarro, *Nat. Commun.*, 2017, **8**, 14457.
- 46 E. López-Maya, C. Montoro, V. Colombo, E. Barea and J. A. R. Navarro, *Adv. Funct. Mater.*, 2014, **24**, 6130–6135.
- 47 M. Mon, E. Tiburcio, J. Ferrando-Soria, R. G. San Millan, J. A. R. Navarro, D. Armentano and E. Pardo, *Chem. Commun.*, 2018, **54**, 9063–9066.
- 48 (a) Y. Yuan, J. Li, X. Sun, G. Li, Y. Liu, G. Verma and S. Ma, *Chem. Mater.*, 2019, **31**, 1084–1091; (b) J. Hou,



- M. L. R. Gómez, A. Krajnc, A. McCaul, S. Li, A. M. Bumstead, A. F. Sapnik, Z. Deng, R. Lin, P. A. Chater, D. S. Keeble, D. A. Keen, D. Appadoo, B. Chan, V. Chen, G. Mali and T. D. Bennett, *J. Am. Chem. Soc.*, 2020, **142**(8), 3880–3890; (c) L.-M. Yang, G.-Y. Fang, J. Ma, R. Pushpa and E. Ganz, *Phys. Chem. Chem. Phys.*, 2016, **18**, 32319–32330; (d) M. Kalaj, M. R. Momeni, K. C. Bentz, K. S. Barcus, J. M. Palomba, F. Paesani and S. M. Cohen, *Chem. Commun.*, 2019, **55**, 3481–3484.
- 49 A. Karmakar, A. V. Desai and S. K. Ghosh, *Coord. Chem. Rev.*, 2016, **307**, 313–341.
- 50 X. Suo, Y. Yu, S. Qian, L. Zhou, X. Cui and H. Xing, *Angew. Chem., Int. Ed.*, 2021, **60**, 1–7.
- 51 X. Cui, Q. Yang, L. Yang, R. Krishna, Z. Zhang, Z. Bao, H. Wu, Q. Ren, W. Zhou, B. Chen and H. Xing, *Adv. Mater.*, 2017, **29**, 1606929.
- 52 M. R. Tchalala, P. M. Bhatt, K. N. Chappanda, S. R. Tavares, K. Adil, Y. Belmabkhout, A. Shkurenko, A. Cadiau, N. Heymans, G. De Weireld, G. Maurin, K. N. Salama and M. Eddaoudi, *Nat. Commun.*, 2019, **10**, 1328.
- 53 T. M. M. Ntep, H. Breitzke, L. Schmolke, C. Schlüsener, B. Moll, S. Millan, N. Tannert, I. E. Aita, G. Buntkowsky and C. Janiak, *Chem. Mater.*, 2019, **31**, 8629–8638.
- 54 W. Jaeschke, H. Claude and J. Herrmann, *J. Geophys. Res.*, 1980, **85**, 5639–5644.
- 55 (a) O. A. Habeeb, R. Kanthasamy, G. A. M. Ali, S. Sethupathi and R. B. M. Yunus, *Rev. Chem. Eng.*, 2018, **34**, 837–854; (b) G. E. Likens, R. F. Wright, J. N. Galloway and T. J. Butler, *Sci. Am.*, 1979, **241**, 43–51.
- 56 R. O. Beauchamp, J. S. Bus, J. A. Popp, C. J. Boreiko, D. A. Andjelkovich and P. Leber, *CRC Crit. Rev. Toxicol.*, 1984, **13**, 25–97.
- 57 M. S. Shah, M. Tsapatsis and J. I. Siepmann, *Chem. Rev.*, 2017, **117**, 9755–9803.
- 58 A. Ros, M. A. Montes-Moran, E. Fuente, D. M. Nevskaja and M. J. Martin, *Environ. Sci. Technol.*, 2006, **40**, 302–309.
- 59 M. Bui, C. S. Adjiman, A. Bardow, E. J. Anthony, A. Boston, S. Brown, P. S. Fennell, S. Fuss, A. Galindo, L. A. Hackett, J. P. Hallett, H. J. Herzog, G. Jackson, J. Kemper, S. Krevor, G. C. Maitland, M. Matuszewski, I. S. Metcalfe, C. Petit, G. Puxty, J. Reimer, D. M. Reiner, E. S. Rubin, S. A. Scott, N. Shah, B. Smit, J. P. M. Trusler, P. Webley, J. Wilcox and N. Mac Dowell, *Energy Environ. Sci.*, 2018, **11**, 1062–1176.
- 60 C. Petit, B. Mendoza and T. J. Bandosz, *ChemPhysChem*, 2010, **11**, 3678–3684.
- 61 M. Khabazipour and M. Anbia, *Ind. Eng. Chem. Res.*, 2019, **58**, 22133–22164.
- 62 L. Hamon, C. Serre, T. Devic, T. Loiseau, F. Millange, G. Férey and G. De Weireld, *J. Am. Chem. Soc.*, 2009, **131**, 8775–8777.
- 63 J. Liu, Y. Wei, P. Li, Y. Zhao and R. Zou, *J. Phys. Chem. C*, 2017, **121**, 13249–13255.
- 64 Y. Belmabkhout, R. S. Pillai, D. Alezi, O. Shekhah, P. M. Bhatt, Z. Chen, K. Adil, S. Vaesen, G. De Weireld, M. Pan, M. Suetin, A. J. Cairns, V. Solovyeva, A. Shkurenko, O. E. Tall, G. Maurin and M. Eddaoudi, *J. Mater. Chem. A*, 2017, **5**, 3293–3303.
- 65 (a) J. Izumi, T. Morimoto, H. Tsutaya and K. Araki, *Stud. Surf. Sci. Catal.*, 1993, **80**, 293–299; (b) P. B. S. Rallapalli, K. Cho, S. H. Kim, J.-N. Kim and H. C. Yoon, *Fuel*, 2020, **281**, 118985.
- 66 P. Lyn and G. Maurin, *ACS Appl. Mater. Interfaces*, 2021, **13**, 4813–4822.
- 67 L. Hamon, C. Serre, T. Devic, T. Loiseau, F. Millange, G. Férey and G. De Weireld, *J. Am. Chem. Soc.*, 2009, **131**, 8775–8777.
- 68 E. Sánchez-González, P. G. M. Mileo, M. Sagastuy-Breña, J. R. Álvarez, J. E. Reynolds III, A. Villareal, A. Gutiérrez-Alejandre, J. Ramírez, J. Balmaseda, E. González-Zamora, G. Maurin, S. M. Humphrey and I. A. Ibarra, *J. Mater. Chem. A*, 2018, **6**, 16900–16909.
- 69 J. A. Zárate, E. Sánchez-González, T. Jurado-Vázquez, A. Gutiérrez-Alejandre, E. González-Zamora, I. Castillo, G. Maurin and I. A. Ibarra, *Chem. Commun.*, 2019, **55**, 3049–3052.
- 70 J. G. Flores, J. A. Zárate-Colín, E. Sánchez-González, J. R. Valenzuela, J. A. Gutiérrez-Alejandre, J. Ramírez, V. Jancik, J. Aguilar-pliego, M. C. Zorrilla, H. A. Lara-García, E. González-Zamora, G. Guzmán-González, I. González, G. Maurin and I. A. Ibarra, *ACS Appl. Mater. Interfaces*, 2020, **12**, 18885–18892.
- 71 Y. V. Mikhaylik and J. R. Akridge, *J. Electrochem. Soc.*, 2004, **151**, A1969–A1976.
- 72 D. Moy, A. Manivannan and S. R. Narayanan, *J. Electrochem. Soc.*, 2015, **162**, A1–A7.
- 73 A. B. Andreeva, K. N. Le, L. Chen, M. E. Kellman, C. H. Hendon and C. K. Brozek, *J. Am. Chem. Soc.*, 2020, **142**, 19291–19299.
- 74 E. S. Grape, J. G. Flores, T. Hidalgo, E. Martínez-Ahumada, A. Hautier, D. R. Williams, M. O. Kee, O. Lars, T. Willhammar, P. Horcajada, I. A. Ibarra and A. K. Inge, *J. Am. Chem. Soc.*, 2020, **142**, 16795–16804.
- 75 H. Wang, X. Zeng, W. Wang and D. Cao, *Chem. Eng. Sci.*, 2015, **135**, 373–380.
- 76 K. Polychronopoulou, J. L. G. Fierro and A. M. Efstathiou, *Appl. Catal., B*, 2005, **57**, 125–137.
- 77 X. Liu and R. Wang, *J. Hazard. Mater.*, 2017, **326**, 157–164.
- 78 L. Sigot, G. Ducom and P. Germain, *Chem. Eng. J.*, 2016, **287**, 47–53.
- 79 X. Wang, X. Ma, X. Xu, L. Sun and C. Song, *Top. Catal.*, 2008, **49**, 108–117.
- 80 X. Ma, X. Wang and C. Song, *J. Am. Chem. Soc.*, 2009, **131**, 5777–5783.
- 81 F. Adib, A. Bagreev and T. J. Bandosz, *Langmuir*, 2000, **16**(4), 1980–1986.
- 82 H. Dong, Q. Zhou, L. Zhang and Y. Tian, *Angew. Chem., Int. Ed.*, 2019, **58**, 13948–13953.
- 83 R. Motterlini and L. E. Otterbein, *Nat. Rev. Drug Discovery*, 2010, **9**, 728–743.
- 84 G. Yang, L. Wu, B. Jiang, W. Yang, J. Qi, K. Cao, Q. Meng, A. K. Mustafa, W. Mu, S. Zhang, S. H. Snyder and R. Wang, *Science*, 2008, **322**, 587–590.





- 85 D. J. Polhemus and D. J. Lefer, *Circ. Res.*, 2014, **114**, 730–737.
- 86 M. N. Hughes, M. N. Centelles and K. P. Moore, *Free Radical Biol. Med.*, 2009, **47**, 1346–1353.
- 87 C. Szabo and A. Papapetropoulos, *Pharmacol. Rev.*, 2017, **69**, 497–564.
- 88 H. A. Henthorn and M. D. Pluth, *J. Am. Chem. Soc.*, 2015, **137**(48), 15330–15336.
- 89 D.-W. Li, L.-L. Qu, K. Hu, Y.-T. Long and H. Tian, *Angew. Chem.*, 2015, **127**, 12949–12952.
- 90 C. Yang, X. Yin, S.-Y. Huan, L. L. Chen, X.-X. Hu, M.-Y. Xiong, K. Chen and X.-B. Zhang, *Anal. Chem.*, 2018, **90**, 3118–3123.
- 91 J. Yang and Y. W. Yang, *Small*, 2020, **16**, 1906846.
- 92 P. K. Allan, P. S. Wheatley, D. Aldous, M. Infas, C. Tang, J. A. Hriljac, I. L. Megson, K. W. Chapman, G. D. Weireld, S. Vaesen and R. E. Morris, *Dalton Trans.*, 2012, **41**, 4060–4066.
- 93 H. Li, X. Feng, Y. Guo, D. Chen, R. Li, X. Ren, X. Jiang, Y. Dong and B. Wang, *Sci. Rep.*, 2014, **4**, 4366.
- 94 Y. Ma, H. Su, X. Kuang, X. Li, T. Zhang and B. Tang, *Anal. Chem.*, 2014, **86**, 11459–11463.
- 95 S. Nandi, S. Banesh, V. Trivedi and S. Biswas, *Analyst*, 2018, **143**, 1482–1491.
- 96 X. Zhang, L. Fang, K. Jiang, H. He, Y. Yang, Y. Cui, B. Li and G. Qian, *Biosens. Bioelectron.*, 2019, **130**, 65–72.
- 97 C. Yang, K. Chen, M. Chen, X. Hu, S. Y. Huan, L. Chen, G. Song and X. B. Zhang, *Anal. Chem.*, 2019, **91**, 2727–2733.
- 98 Y. Li, J. Zhou, L. Wang and Z. Xie, *ACS Appl. Mater. Interfaces*, 2020, **12**, 30213–30220.
- 99 C. D. Demirhan, W. W. Tso, J. B. Powell and E. N. Pistikopoulos, *AIChE J.*, 2019, **65**, e16498.
- 100 (a) A. Fangmaier, A. Hadwiger-Fangmaier, L. Van der Eerden and H. J. Jäger, *Environ. Pollut.*, 1994, **86**, 43–82; (b) S. N. Behera, M. Sharma, V. P. Aneja and R. Balasubramanian, *Environ. Sci. Pollut. Res.*, 2013, **20**, 8092–8131.
- 101 R. Metkemeijer and P. Achard, *J. Power Sources*, 1994, **49**, 271–282.
- 102 Z. Tamainot-Telto, S. J. Metcalf, R. E. Critoph, Y. Zhong and R. Thorpe, *Int. J. Refrig.*, 2009, **32**, 1212–1229.
- 103 (a) C. Petit, B. Mendoza and T. J. Bandosz, *Langmuir*, 2010, **26**, 15302–15309; (b) M. J. Katz, A. J. Howarth, P. Z. Moghadam, J. B. DeCoste, R. Q. Snurr, J. T. Hupp and O. K. Farha, *Dalton Trans.*, 2016, **45**, 4150–4153.
- 104 D. W. Kang, S. E. Ju, D. W. Kim, M. Kang, H. Kim and C. S. Hong, *Adv. Sci.*, 2020, **16**, 2002142.
- 105 J. Helminen, J. Helenius, E. Paatero and I. Turunen, *J. Chem. Eng. Data*, 2001, **46**, 391–399.
- 106 (a) C. Petit and T. J. Bandosz, *Adv. Funct. Mater.*, 2010, **20**, 111–118; (b) D. Britt, D. Tranchemontagne and O. M. Yagui, *Proc. Natl. Acad. Sci. U. S. A.*, 2008, **105**, 11623–11627.
- 107 A. J. Rieth, Y. Tulchinsky and M. Dincă, *J. Am. Chem. Soc.*, 2016, **138**, 9401–9404.
- 108 A. J. Rieth and M. Dincă, *J. Am. Chem. Soc.*, 2018, **140**, 3461–3466.
- 109 D. W. Kim, D. W. Kang, M. Kang, J.-H. Lee, J. H. Choe, Y. S. Chae, D. S. Choi, H. Yun and C. S. Hong, *Angew. Chem.*, 2020, **59**, 22531–22536.
- 110 H. G. W. Godfrey, I. da Silva, L. Briggs, J. H. Carter, C. G. Morris, M. Savage, T. L. Easun, P. Manuel, C. A. Murray, C. C. Tang, M. D. Frogley, G. Cinque, S. Yang and M. Schröder, *Angew. Chem., Int. Ed.*, 2018, **57**, 14778–14781.
- 111 X. Han, W. Lu, Y. Chen, I. Silva, J. Li, L. Lin, W. Li, A. M. Sheveleva, H. G. W. Godfrey, Z. Lu, F. Tuna, E. J. L. McInnes, Y. Cheng, L. L. Daemen, L. J. M. McPherson, S. J. Teat, M. D. Frogley, S. Rudic, P. Manuel, A. J. Ramirez-cuesta, S. Yang and M. Schröder, *J. Am. Chem. Soc.*, 2021, **143**(8), 3153–3161.
- 112 T. Yoskamtorn, P. Zhao, X.-P. Wu, K. Purchase, F. Orlandi, P. Manuel, J. Taylor, Y. Li, S. Day, L. Ye, C. C. Tang, Y. Zhao and S. C. E. Tsang, *J. Am. Chem. Soc.*, 2021, **143**(8), 3205–3218.
- 113 P. Zhao, H. Fang, S. Mukhopadhyay, A. Li, S. Rudic, I. J. McPherson, C. C. Tang, D. Fairen-Jimenez, S. C. E. Tsang and S. A. T. Redfern, *Nat. Commun.*, 2019, **10**, 999.
- 114 F. Gholami, M. Tomas, Z. Gholami and M. Vakili, *Sci. Total Environ.*, 2020, **714**, 136712.
- 115 D. Krewski, M. Jerrett, R. T. Burnett, R. Ma, E. Hughes, Y. Shi, M. C. Turner, C. A. Pope, G. Thurston, E. E. Calle, M. J. Thun, B. Beckerman, P. DeLuca, N. Finkelstein, K. Ito, D. K. Moore, K. B. Newbold, T. Ramsay, Z. Ross, H. Shin and B. Tempalski, *Res. Rep. Health Eff. Inst.*, 2009, 5–114; discussion 115–136.
- 116 S. Safieddine, C. Clerbaux, M. George, J. Hadji-Lazaro, D. Hurtmans, P.-F. Coheur, C. Wespes, D. Loyola, P. Valks and N. Hao, *J. Geophys. Res. Atmos.*, 2013, **118**, 10 555–10 566.
- 117 F. Rezaei, A. A. Rownaghi, S. Monjezi, R. P. Lively and C. W. Jones, *Energy Fuels*, 2015, **29**, 5467–5486.
- 118 J. Despres, M. Koebel, O. Kröcher, M. Elsener and A. Wokaun, *Microporous Mesoporous Mater.*, 2003, **58**, 175–183.
- 119 X. Chang, G. Lu, Y. Guo, Y. Wang and Y. Guo, *Microporous Mesoporous Mater.*, 2013, **165**, 113–120.
- 120 W. J. Zhang, S. Rabiei, A. Bagreev, M. S. Zhuang and F. Rasouli, *Appl. Catal., B*, 2008, **83**, 63–71.
- 121 N. Gargiulo, A. Peluso and D. Caputo, *Processes*, 2020, **8**, 613.
- 122 J.-R. Li, R. J. Kuppler and H.-C. Zhou, *Chem. Soc. Rev.*, 2009, **38**, 1477–1504.
- 123 G. W. Peterson, J. J. Mahle, J. B. DeCoste, W. O. Gordon and J. A. Rossin, *Angew. Chem., Int. Ed.*, 2016, **55**, 6235–6238.
- 124 X. Han, H. G. W. Godfrey, L. Briggs, A. J. Davies, Y. Cheng, L. L. Daemen, A. M. Sheveleva, F. Tuna, E. J. L. McInnes, J. Sun, C. Drathen, M. W. George, A. J. Ramirez-Cuesta, K. M. Thomas, S. Yang and M. Schröder, *Nat. Mater.*, 2018, **17**, 691–696.
- 125 X. Han, Y. Hong, Y. Ma, W. Lu, J. Li, L. Lin, A. M. Sheveleva, F. Tuna, E. J. L. McInnes, C. Dejoie, J. Sun, S. Yang and M. Schröder, *J. Am. Chem. Soc.*, 2020, **142**, 15235–15239.



- 126 A. M. Wright, C. Sun and M. Dincă, *J. Am. Chem. Soc.*, 2021, **143**, 681–686.
- 127 B. Xiao, P. S. Wheatley, X. Zhao, A. J. Fletcher, S. Fox, A. G. Rossi, I. L. Megson, S. Bordiga, L. Regli, K. M. Thomas and R. E. Morris, *J. Am. Chem. Soc.*, 2007, **129**, 1203–1209.
- 128 S. M. Vornholt, M. J. Duncan, S. J. Warrender, R. Semino, N. A. Ramsahye, G. Maurin, M. W. Smith, J.-C. Tan, D. N. Miller and R. E. Morris, *ACS Appl. Mater. Interfaces*, 2020, **12**, 58263–58276.
- 129 A. C. McKinlay, B. Xiao, D. S. Wragg, P. S. Wheatley, I. L. Megson and R. E. Morris, *J. Am. Chem. Soc.*, 2008, **130**, 10440–10444.
- 130 (a) M. O. Andreae and P. Merlet, *Global Biogeochem. Cycles*, 2001, **15**, 955–966; (b) J.-Y. Lee, T. C. Keener and Y. J. Yang, *J. Air Waste Manage. Assoc.*, 2009, **59**, 725–732.
- 131 (a) G. V. Last and M. T. Schmick, *Identification and Selection of Major Carbon Dioxide Stream Compositions*, US Department of Energy, Pacific Northwest National Laboratory, Washington U. S. A., 2011; (b) R. Zevenhoven and P. Kilpinen, in *Control of Pollutants in Flue Gases and Fuel Gases*, Helsinki Univ. of Technology, Otaniemi (Finland). Energy Engineering and Environmental Protection, Finland, 2005, ch. 2, pp. 2–4.
- 132 J. H. Carter, X. Han, F. Y. Moreau, I. da Silva, A. Nevin, H. G. W. Godfrey, C. C. Tang, S. Yang and M. Schröder, *J. Am. Chem. Soc.*, 2018, **140**, 15564–15567.
- 133 Y. Zhang, P. Zhang, W. Yu, J. Zhang, J. Huang, J. Wang, M. Xu, Q. Deng, Z. Zeng and S. Deng, *ACS Appl. Mater. Interfaces*, 2019, **11**(11), 10680–10688.
- 134 Y. L. Fan, H. P. Zhang, M. J. Yin, R. Krishna, X. F. Feng, L. Wang, M. B. Luo and F. Luo, *Inorg. Chem.*, 2021, **60**(1), 4–8.
- 135 L. J. Gou, X. F. Feng, Z. Gao, R. Krishna and F. Luo, *Inorg. Chem.*, 2021, **60**(3), 1310–1314.
- 136 M. J. Yin, X. H. Xiong, X. F. Feng, W. Y. Xu, R. Krishna and F. Luo, *Inorg. Chem.*, 2021, **60**(5), 3447–3451.
- 137 Y. Belmabkhout, P. M. Bhatt, K. Adil, R. S. Pillai, A. Cadiau, A. Shkurenko, G. Maurin, G. Liu, W. J. Koros and M. Eddaoudi, *Nat. Energy*, 2018, **3**, 1059–1066.
- 138 S. Vaesen, V. Guillermin, Q. Yang, A. D. Wiersum, B. Marszalek, B. Gil, A. Vimont, M. Daturi, T. Devic, P. L. Llewellyn, C. Serre, G. Maurin and G. De Weireld, *Chem. Commun.*, 2013, **49**, 10082–10084.
- 139 P. M. Bhatt, Y. Belmabkhout, A. H. Assen, L. J. Weselinski, H. Jiang, A. Cadiau, D.-X. Xue and M. Eddaoudi, *Chem. Eng. J.*, 2017, **324**, 392–396.
- 140 Z. Li, Y. Xiao, W. Xue, Q. Yang and C. Zhong, *J. Phys. Chem. C*, 2015, **119**(7), 3674–3683.
- 141 E. N. H. S. Vaese and G. De Weireld, *Microporous Mesoporous Mater.*, 2012, **154**, 93–99.
- 142 J. Xu, W. Xing, H. Wang, W. Xu, Q. Ding, L. Zhao, W. Guo and Z. Yan, *J. Mater. Sci.*, 2016, **51**, 2307–2319.
- 143 A. G. P. Maloney, P. A. Wood, S. C. Ward and D. Fairen-Jimenez, *Chem. Mater.*, 2017, **29**, 2618–2625.
- 144 D. Ongari, L. Talirz and B. Smit, *ACS Cent. Sci.*, 2020, **6**(11), 1890–1900.
- 145 A. J. Howarth, Y. Liu, P. Li, Z. Li, T. C. Wang, T. T. Hupp and O. K. Farha, *Nat. Rev. Mater.*, 2016, **1**, 15018.

